FACULTY OF SCIENCES AND TECHNOLOGY
DEPARTMENT OF PHYSICS

UNIVERSITY OF COIMBRA

3D Heart Reconstruction

Diogo Roxo

Coimbra,2011

Faculty of Science and Technology, University of Coimbra

Partnership:

Department of Physics (DF)

Department of Electrical and Computer Engineering (DEEC)

Diogo Roxo

Thesis submitted for the degree of Integrated Master in Biomedical Engineering

Oriented by:

PhD José Silva (DF), PhD Jaime Santos (DEEC), PhD Rui Cortesão(DEEC)

September, 2011

Contents

List of Figures

List of Tables

Acknowledgements

A partnership between the University of Coimbra and two hospitals allowed the development of this project. The main intervenients were the Department of Physics(DF), the Department of Electrical and Computer Engineering(DEEC), the Pediatric Hospital of Coimbra and the University Hospital of Coimbra. The cooperation from both hospitals was crucial to achieve a reliable validation of the level set segmentation method. Equally crucial was the tele-echocardiography system of the Institute of Systems and Robotics at the DEEC to obtain a 3D reconstruction of a heart phantom.

This work was supported in part by the Portuguese Science and Technology Foundation (FCT) Project PTDC/EEA-CRO/110008/2009.

First of all I would like to thank my advisors for all the support given. I would also like to thank the physicians of the pediatric hospital and of the University Hospital of Coimbra for the all the patience and images that made this work possible.

Especially thanks to all my family for being there since I can remember and to my friends that made these five years in the University of Coimbra the best experience of my live.

.

Abstract

The purpose of this thesis was to achieve a 3D reconstruction of the four heart chambers using 2D echocardiographic images. A level set algorithm based on the phase symmetry approach and on a new logarithmic based stopping function was used to extract simultaneously the four heart cavities from these images in a fully automatic way. However to proceed to the 3D reconstruction using the segmented images, it was first necessary to satisfy clinical practise requirements. This means that the algorithm had to be validated to access the performance of the segmentation. Regarding this, the framework of this thesis was divided in two parts: validation of the segmentation algorithm and 3D reconstruction. The contours obtained in the segmentation were compared with the ones obtained by four physicians to evaluate the performance, reliability and confidence for eventual clinical practice. That algorithm evaluation versus clinicians' performance was made using eleven figures of merit: *Mean/Max/Larger than 5 pixels Distance*, *Pratt Function*, *Hausdorff Distance*, *Similarity Angle*, *Similarity Region*, *Accuracy*, *Overlap*, *Sensitivity* and *Specificity*; and two statistical tools: Box-plots and Dendrograms. The results indicate a reliable performance of the level set method for all chambers. The evaluation was based on echocardiography images of children. The 3D reconstruction was achieved using a heart phantom. This phantom was mainly composed by four balloons attached together and submerged in a water environment. A robotic arm with an ultrasound probe attached was used to take a large number of frames from the heart phantom. Several attempts were made using two types of acquisition: in Rotation and in Translation. Offline reconstructions of two rotations and one translation were presented and analyzed. The results of the rotations were far better than the translation. It was possible to infer the shape and volume of the balloons. These results present one more step in the way for a real-time 3D reconstruction using a tele-echographic system.

Chapter 1

Introduction

Congenital heart diseases are present in 8 of every 1000 newborns. The diagnosis of these pathologies usually depend on the imaging methods available. In this context, echocardiography plays an important role being non-invasive, low-cost and portable allowing to diagnose congenital abnormalities and assess the cardiac function in a real-time dynamic observation. A correct diagnosis requires a close observation of the heart chambers, wall motions, valves function and an estimation of the cavities volumes.

1.1. Motivation

An ultrasound examination requires a physician with good hand-eye coordination and capable of integrate the acquired information over time and space. These abilities are essential to mentally visualize a 3D representation of a heart chamber from the 2D images while performing movements with the ultrasound probe. However specialized physicians with this kind of training are not available in every healthcare centres, lacking in emergency situations when they can be of most help.

A good alternative to conventional care and a way to solve some of these problems is what has been called of remote-appointment, a non-local diagnostic system

which enables to examine a patient not present physically. In some cases this appears to be the only possible solutions to solve a lack of specialized physicians. However the ultimate goal of this project goes beyond this, create a 3D imaging technique using ultrasound equipment which would not require a specialized physician performing the exam. A robotized tele-Echocardiography were a robot would perform an automatic acquisition. Then image processing techniques as a 2D segmentation cardiac chambers followed by a 3D reconstruction would be applied to the acquired images, providing a detailed 3D visualization of the heart cavities. However extracting the cavities from 2D ultrasound images has revealed to be a hard task, since echocardiographic images have low spatial resolution, high level of speckle noise and a tendency to present artifacts shadowing and attenuation. All these limitations influence greatly a clear visualization of the heart boundaries requiring once again an expert to trace them.

Due to the subjectivity of these estimations, a considerable variability is found between specialized physicians. In order to proceed to the 3D reconstruction it's essential to have a segmentation method that presents a behavior similar to a specialized physician. An extensive validation is essential to access the performance of the segmentation method. This can only be achieved by studying the inter/intra physicians variability for a large number of echocardiographic images and then compare it the physicians versus segmentation method variability. The cooperation of several physicians from different hospitals is also essential.

A segmentation method that allowed a valid 3D reconstruction of the cardiac chambers could also substantially support an efficient and safe clinical diagnosis in also emerging areas such as image-guided interventions and therapy that requires high-resolution images to visualize the heart with some detail[2,3].

1.2. Objectives

The contours drawn by expert physicians are essential to perform a reliable validation. A manual acquisition is a time consuming task and is subject to considerable precision errors. The first objective is the development of an user-friendly interface where the contours are drawn directly in the computer greatly reducing the acquisition errors.

One of the objectives of this project is to make an inter/intra-observer evaluation and subsequently validate a segmentation method of the four heart chambers. The goal is to demonstrate that the automatic segmentation(performed by this method) is equivalent to hand segmentation provided by medical experts.

Furthermore, it‘s intended to proceed to the acquisition of sequential images of a heart phantom using a robot, then segment these images (using the algorithm already developed) and finally proceed to the 3D reconstruction of the heart phantom from the 2D images.

1.3. Structure of the Thesis

The first chapter gives a general introduction of this work. Chapter 2 proceeds making an overview of the heart anatomy and congenital defects. Then the physical and technical principles of Echocardiography are introduced, focusing in the image generation through wave propagation and reflection. Chapter 3 presents an overview of the existent segmentation methods in ultrasound imaging and a detailed explanation of the level set segmentation used. In chapter 4 the framework of the evaluation is introduced focusing in the contours acquisition first, the validation methodology, the figures of merit and statistical tools used. The results of the validation are presented in Chapter 5. Chapter 6 and 7 are related the 3D reconstruction. The first one starts with an overview of the tele-Ecography systems existent today. Then the tele-Echocardiographic system used in this work and the associated robotic manipulation principles are introduced. This thesis concludes in Chapter 8 with a review of the results obtained and the future work that needs to be done mainly in 3D heart reconstruction.

1.4. Publications

During this year, a full paper was submitted and accepted in an International Conference (HCIST). It will be published by Springer-Verlag in a CCIS series book, which is abstracted/indexed in ISI proceedings and SCOPUS.

The International workshop on Health and Social Care Information Systems and Technologies will be held in Vilamoura. The paper presents an evaluation of performance of an Automatic segmentation method of the four heart cavities in relation to contours acquired from four physicians.

The material of this thesis will be also used to write a paper and submit to a scientific journal in the area Ultrasound Imaging.

Chapter 2

Theoretical Background

This chapter gives an overview of all theoretical principles associated to Echocardiographic imaging. It starts by describing the heart anatomy/physiology and the most common pathologies associated to congenital malformations. Then it explains the physical principles and functioning of the ultrasound equipment used in standard echocardiography. This imaging modality has a very important place in clinical practise for many good reasons: easy and fast to use giving anatomical information in real time, non-invasive and low cost. It enables a physician to collect information not only of the cavities size, shape, wall motion but also myocardial and blood velocities based on the Doppler shift.

2.1 Overview of the heart

The heart is an organ that functions by pumping blood through the entire body. it's composed by several layers of cardiac muscle allowing quick contractions while the all the other hollow organs are composed by smooth muscle. Both muscle types contract involuntarily causing muscle cells to shorten while skeletal muscle, the major

component of body mass, contracts voluntarily waiting for a signal from brain to react. Smooth and Cardiac muscle may be functionally similar, however in a close observation Cardiac muscle resembles more to skeletal muscle. Both of them are striated allowing a quicker contraction comparing to smooth muscle. When the cardiac muscle is stretched beyond their normal resting capacity (like ventricles filled with blood) a more powerful contraction is generated. The cardiac muscle is called myocardium, internally it's covered by the endocardium and externally by the pericardium[36].

The heart is located between the lungs behind the sternum, it weighs between 200 and 425 grams and it's a little larger than the size of a fist. It is composed by four chambers. The upper chambers are named right and left atria while the lower chambers right and left ventricles. The septum (a muscle of wall) and the heart valves (tricuspid and mitral) are located between them. The atria receive blood from the veins and the ventricles pump the blood back to the body. There are two types of circulation referred as pulmonary and systemic circuits. In the pulmonary circulation deoxygenated blood leaves the heart through the pulmonary artery, connected to the right ventricle, heading to the lungs. In the lungs it becomes oxygenated and returns to heart, through the pulmonary veins, entering the left atrium. In the systemic circulation the oxygenated blood leaves the heart through the aorta, connected to the left ventricle, heading to all the organs in the body. Then it returns to the heart through the superior and inferior vena cava penetrating the right atrium.

The left ventricle is the largest and strongest chamber thus it's responsible to push the blood through the aortic valve. [37] The cardiac chambers and circulatory circuits described are visible in Figure 2.1a. The contractions are caused by electrical impulses. As the blood fills the right and left atria, the senatorial node sends out an electrical signal. This causes the contraction of the atria pushing the blood through the tricuspid and mitral valve into the ventricles. This is called **diastole** (Figure 2.1b) and it's the first of two-part pumping phase. When the ventricles are full of blood the second part begins. The electrical signals travel to the ventricles along a pathway of cells. The contraction caused in the ventricles is called **systole**(Figure 2.1b). The blood leaves the ventricles through the pulmonary and aortic valves while the tricuspid and mitral valves remain close to prevent a back flow of blood. After this the ventricles relax closing the pulmonary and aortic valves.

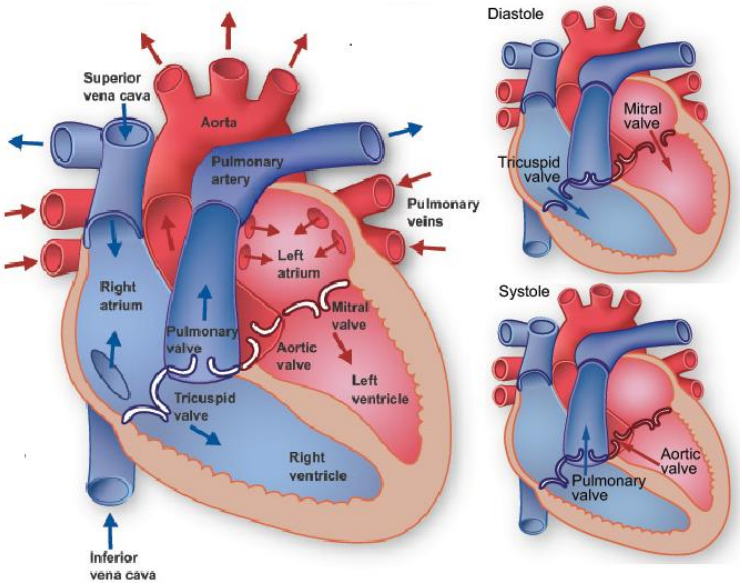

a) **b)**

Figure 2.1 – Oxygenated blood is represented in red and deoxygenated in blue a)Heart anatomy b) Diastole and systole[38].

The lower pressure causes the opening of the mitral and tricuspid valves and the cycle begin one more time. This cycle is called a heartbeat and it happens 60-80 times a minute at rest however variations may occur[38].

2.1.1 Congenital heart defect

Congenital heart defect is the most frequent disease of all major birth defects. This occurs when the heart or the blood vessels around it did not develop normally before birth. The most commons are the Septal defects than occurs when a hole is present in the wall (septum) that separates the right from the left side of the heart allowing mixing of blood. This can occur between the two atria(as shown is figure 2.2) or the two ventricles.

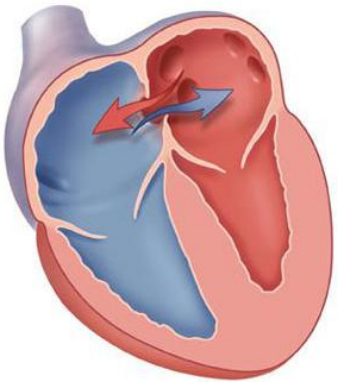

Figure 2.2 – Atrial Septal defect[39].

Small holes don’t cause problems and will probably close on their own during growth. Large holes (mainly between ventricles) can make the heart work too hard, increasing the blood pressure in the right side of the heart and lungs.

The blood follow is controlled by the heart valves. Some heart defects are related with a malfunctioning of these valves like when they do not open or close completely limiting the blood circulation [39].

The atria and ventricles shape attributes, like thickness, wall motion and cavities area permit a quantitative measure the cardiac function which is a critical step in the detection of a heart failure. The chamber volumes in the end of the systole and diastole, the pressure-volume ratio and the left ventricle ejection fraction allow to perform a diagnostic. Echocardiography is essential to access all of this information.

2.2 Echocardiography

Echocardiography is an important tool used in medical diagnosis. It uses ultrasound waves to produce images of a beating heart. A piezoelectric transducer emits ultrasound waves through the chest and then detects the reflections as they return from the heart. In figure 2.3 a standard ultrasound equipment is represented.

Figure 2.3 – Standard ultrasound scanner with 2 transducers.[48].

Observing the wall motions and shape changes of the heart chambers allow to access the cardiac function. When changes consistently appear in these patterns it’s possible to detect several heart diseases. Due to the advantages demonstrated over other

diagnostic tools it has become a frequently used method to evaluate the heart. It is painless, safe (has no known harmful biological effects allowing it to be repeated indefinitely), easily transportable, real-time observation.

The probe used to scan the heart consists in a phased-array transducer. A signal processing box is used to reconstruct the reflected signals and the resulting image is displayed on a monitor.

2.2.1 Transducers

The transducer used in echocardiography is composed by piezoelectric crystals. It is subjected to an alternating electrical current that excites the crystals independently producing ultrasonic waves. The frequency range of these waves is 1 to 40 MHz and they are emitted as short pulses of 1 μs with an interval of 100 to 200 μs. During this intervals the transducer function is to detect reflections returning from the heart. It converts the mechanical vibrations into an electrical signal and sending it back to the echocardiographic equipment to be displayed. 250 pulses are typically necessary to form a complete 2D frame taking just tens of milliseconds allowing a dynamic observation of the cardiac motion since the duration of one heart beat is somewhere between 0.3 and 1.2 seconds.

The most commonly used is the 1D array transducer and it can be excited using a linear array or a phased-array. This last one used in cardiology due to the small acoustic window of the heart changing the direction of the wave focusing in arbitrary points and allowing to quickly collect more information.

2.2.2 Display Modes (A,B and M)

There are 3 different modes to represent the echoes received from the transducer: A , B and M.

The A-mode (A for amplitude) was the first one to be used in ultrasound devices. It is a 1D scan that displays the signal amplitude on the x axis and the depth (or the time in some cases) on the y axis. The strongest echoes (the peaks of the signal) represent the boundaries between the heart chambers.

The B-mode (B for brightness) consist in consecutive 1D scans consecutively taken through a single plane. The amplitudes of the returning echoes are not represented in an axis as in A-mode. They are displayed in a screen monitor as intensity dots in a

grayscale, proportional to the amplitudes of the echoes. Most echocardiographic equipment today uses between 64 to 512 shades of gray. The biggest value of the scale corresponds to the brightest possible dot. A 2D image is then formed from the consecutive scans using a phased array transducer. This is the mode used in diagnosis and allows to capture more than 40 frames per second allowing a real time observation of a moving structure as the heart.

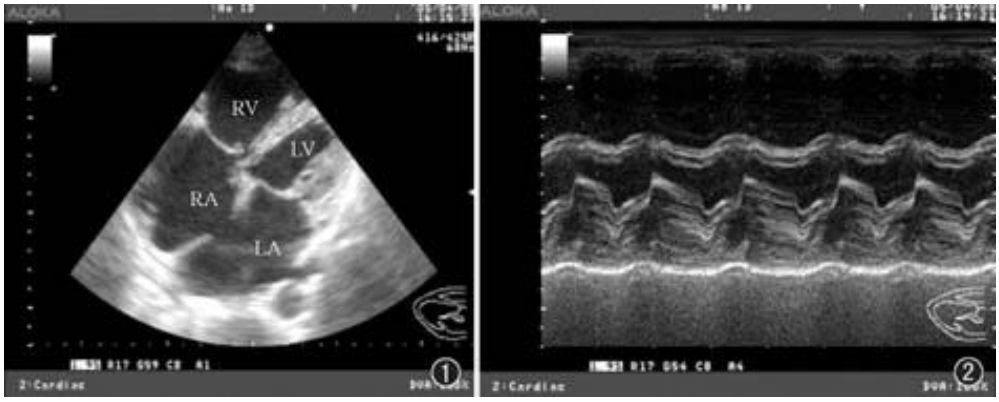

a) b)

Figure 2.4 –Echocardiographic Image of the four heart chambers: a) in B-mode b) in M-mode[49].

In the M-mode (M for motion) the transducer is pointed to the heart displaying the returning echoes in B-mode. A cross section of this image is then selected and the depth of penetration is represented in the y-axis and a time parameter in x-axis. Recording a B-mode continuous acquisition and monitoring the cardiac electrical activity at the same time it's possible to know various anatomical characteristics such as the beginning of the cardiac cycle and the size, thickness and movement of various structures. [41,44]

2.2.3 Principles of ultrasound

The physical principles behind ultrasound behaviour are very important to understand because they allow to collect vital information of the soft tissues in a non-invasive form. Ultrasounds are propagated in waves so its behaviour is given by:

$$\lambda = \frac{c}{f} \qquad (2.1)$$

Where λ, f and c correspond to wavelength, wave frequency and the acoustic velocity of the ultrasound, respectively. The wavelength and frequency are inversely related for any

tissue thus increasing f the wavelength and consequently the minimum distance to visualize two different structures also decreases. The obvious conclusion is that a high resolution is obtained when high frequencies are used. However as frequency increases the wave penetration into soft tissues decreases so it's necessary to find an optimal relation between resolution and penetration. An optimal image is obtained using a frequency that allows an adequate penetration for the highest possible resolution. A high frequency also allows to emit a larger number of wave bursts per second from the transducer improving the spatial resolution. For most soft tissues the acoustic velocity remains constant no matter the wavelength or frequency[42].

To achieve a penetration of at least 24 cm into the chest, transthoracic transducers typical use frequencies between 1.6 to 7.0 MHz. Most of them are broadband allowing to choose a frequency in this range. The qualitative concept of tissue penetration is the ultrasonic attenuation. It varies in every tissue type and is defined as the decrease rate in wave amplitude per penetrated distance for a given frequency. The ultrasonic attenuation depends of two properties, the reflection and the absorption of sound waves. The reflection occurs on the interface of two different tissues and it depends of the acoustic velocity (c) and the tissue density(ρ). The product given by this variables is called acoustic impedance (Z):

$$Z = \rho \times c \qquad (2.2)$$

The image is formed by the reflected ultrasound waves. The impedance increases in very dense structures meaning a raise in reflected waves.

Table 2.1 – Acoustic properties of some tissues[43] at 20º Celcius.

Tissue	Propagation Velocity ($m.s^{-1}$)	Density ($g.mL^{-1}$)	Acoustic Impedance (10^6 rayl[1])
Fat	1480	0.92	1.35
Myocardium	1540	1.07	1.67
Blood	1560	1.06	1.63
Bone	~3000-4000	1.4-1.8	4-6

[1] 1 rayl = $1kg.m^{-2}.s^{-1}$.

In table 2.1 presents the acoustic properties for several materials. The significant difference presented between the air and the other tissues states the importance of placing a gel between the skin and the transducer.

Two types of reflections exists: specular and diffuse. Specular reflections occur on the interface of two different tissues. The greater the difference in acoustic impedance between them the greater the amount of specular echoes. This also means that if more energy is reflected less energy will penetrate the tissue. The diffuse reflections have much less energy. These scattered echoes are produced by much smaller irregularities in the tissues and to "fill the holes" between the specular echoes. Nowadays the most advanced equipments process and analyze the scattered echoes enhancing significantly the image quality[43].

2.2.4 Echo Doppler

The Doppler effect describes the change in wavelength and frequency that occurs when the source waves are moving further or closer to the receiver. When the sound source is stationary in relation to a listener, the wavelength and the frequency remain constant. On the other hand if the sound source is moving toward the listener the wavelength decreases and the frequency increases. The opposite happens if it's moving away.

This principle can be applied in echocardiography to measure the blood follow in valves and in great vessels. It is based in reflected echoes from the red blood cells as they travel through the heart. The transducer emits a continuous beam of ultrasound waves, as the red blood cells move towards the probe the frequency of the reflected echoes will be higher than the transmitted echoes, and vice versa. The difference between transmitted and reflected echoes is called Doppler Shift and it's given by:

$$v = \frac{c\left(f_r - f_t\right)}{2\left(f_t\right)\cos(\alpha)} \tag{2.3}$$

Where v is the blood flow velocity, c is the speed of sound in soft tissue (1540 m/s), f_r is the frequency of the reflected echoes, f_t is the frequency of the transmitted echoes, and α is the *insonation* angle between the direction of blood flow and the ultrasound beam (velocity vector). The Doppler shift is given by $f_r - f_t$ and if positive ($f_r > f_t$) it represents a flow toward the transducer, if negative ($f_r < f_t$) it represents a flow away

from the transducer. The maximal blood flow will be detected when the beam is parallel to the blood flow ($\cos(0^o) = 1$). Since the angle can only be estimated because it's impossible to observe the blood flow in 2D echo, normally the direction of the maximal blood flow is presumed.

Echo Doppler operates in two basic formats, continuous and pulsed wave Doppler. In the first one an ultrasound signal is continuously transmitted and received by different crystals in the transducer. All red blood cells in the overlap region between transmitted and received echoes will contribute to the calculated signal. It's used for an accurate measurement of flow velocities. In pulsed wave Doppler small ultrasound bursts are transmitted at a given frequency with silent intervals between them. The distance of the reflector to the receiver is related to the time that the reflected waves take to return. Using this method it's possible to locate specific regions of an abnormal blood flow still it's is not accurate measuring blood velocities. Several methods exist that display graphically this information, as spectral, colour or power Doppler[43].

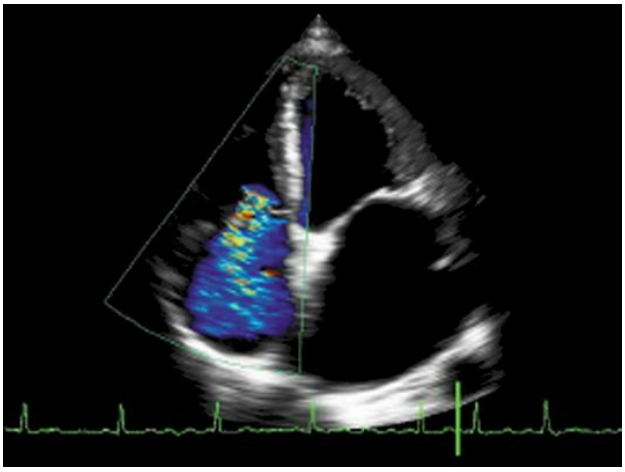

Figure 2.5 – Colour Doppler demonstrating a severe tricuspid regurgitation.

2.2.5 Standard Views

In clinical practise several standard cardiac views are used to perform a qualitative assessment of the structural, anatomical and functional performance and to discover possible abnormalities.

A long axis view is obtained by aligning the transducer in a sagittal orientation. The apical four-chamber view, used in the evaluation, maximizes de left ventricle long axis and the mitral and tricuspid annular dimensions providing a considerable information and the relative sizes of left and right ventricle[47]. Figures 2.5 and 2.6

represent the apical four chamber where the upper regions correspond to the ventricles and the lower regions to the atria. In the left are the right cavities and in the right the left cavities.

2.2.6 Ultrasound Artifacts

Artifacts in ultrasound imaging can appear by various reasons. Sometimes it can be the result of an improper use the equipment by the technician, however the most ordinary situations detected are due to the properties of the human body. Reflections detected by the transducer that, when displayed in a screen, do not correctly represent the anatomical structure under scope are named artifacts. They have several sources and normally are caused by changes in: direction and thickness of propagation, sound velocity, the echo detection and movement between the reflector and the probe. All of these can influence the image quality and even and eliminate structural information.

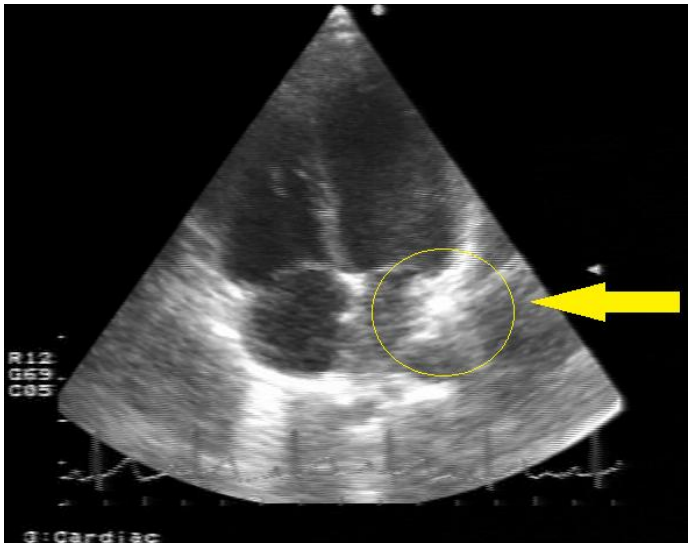

Figure 2.6 – B-mode image with a bright artifact not allowing the correct visualization of the left atrium.

In a B-mode image the artifacts appear as distortions in geometry or signal intensity. An effect known as side lobes is caused when a pulse does not travel purely in one direction creating echoes in the image. A significant amount of artifacts were observed and indentified. The major part are caused when some of the assumptions regarding waves propagation in tissues are not respected. These assumptions are:

- Ultrasound propagation is straight ahead;
- The ultrasound beam as no thickness;
- The echoes come linearly from the reflector to the transducer;

- The echoes belong to the last sound pulse generated;
- The difference in a reflection amplitude are due to the different acoustic impedance of two different tissues.

If this conditions were always respected the image quality will improve. Some measures can be taken to prevent image artifacts like the use of contrast agents or focus the ultrasound beam[45,46].

Although it's not considered an artifact, speckle noise can severely degrade the image quality and difficult the implementation of noise reduction filters. Speckle noise is the cause of a granular appearance in ultrasound images and it's originated from the constructive destructive interference of the reflected pulses from small tissue components [46].

Chapter 3

Level Set Segmentation

Segmentation methods are widely used in different areas with a common purpose: helping in image analysis. In medical domain, it allows to automatically detect a region of interest (ROI), like a tumour or a cavity, and then perform a quantitative evaluation. The level set segmentation method developed by Antunes et al.[2,3] was used to detect the four cardiac cavities in several echocardiographic apical four chamber images. This method, specifically developed for ultrasound B-mode images, was also used to segment ultrasound images from a phantom simulating the four heart chambers.

3.1 Overview of the existent Methods

Today, the larger amount of the existent segmentation methods are still semi-automatic requiring a user interaction in selecting the region of interest[50-52]. Fully automatic segmentation [53] can reduce this intra-physician variability and provide valuable anatomical information about the heart cavities. It's is an essential step to

achieve 3D heart reconstruction, which quality is greatly influenced by the segmentation accuracy and to access the respective cardiac volumes.

The conventional techniques such as region growing or thresholding are quite limited due to the noise present in ultrasound images which makes pre-processing techniques usually indispensable. A large number of noise reduction techniques for echocardiographic images were already implemented, such as Wiener filtering[55], adaptive wavelet thresholding[56] or Bayesian networks filtering[57]. Local phased-based methods were also used since they are not affected by low contrast and speckle.

Jarur et al[58] proposed a method based on a self-organizing map (SOM) for training, using an artificial neural network (figure 3.1). Several authors proposed methods with different pre-processing and segmentation methodologies like Bansod et al[59], optimizing a radial search algorithm to incorporate the temporal information (figure 3.2), or Valdes-Cristerna et al[60] that used a mean shift filter for pre-processing.

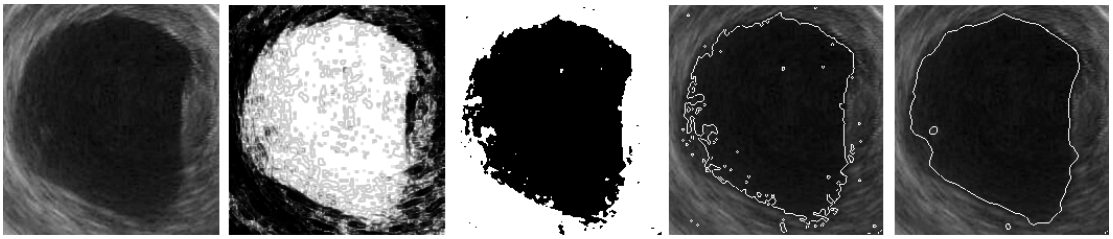

a) **b)** **c)** **d)** **e)**

Figure 3.1 – Jarur segmentation[58] in an echocardiographic intra cavity image: a) Original image, b)Variance based, c) Interior class, d) Edges of interior class, e) Final edge.

Recent segmentation methods based in deformable models (as parametric or geometric models) including level set are used to identify various anatomical structures as cardiac chambers[2,3], lungs[4-6] and vascular or neural networks[7] assisting in the identification of pathologies.

Since the first introduction of snakes by Kass et al [8] active contours have been used for image segmentation and boundary tracking. The basic idea is to start with initial boundary shapes represented in a form of closed curves, i.e. contours, and iteratively modify them by applying shrink/expansion operations according to the constraints of the image.

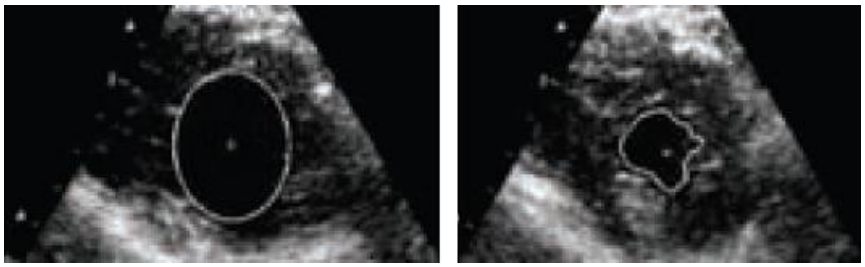

a) **b)**

Figure 3.2 – Bansod segmentation[59]: a) Initialization, first contour, b) Contour determination using a guided local search.

Casseles et al[9] reformulated this methodology in a context of partial differential equations [54](PDE) using the level set framework. The first level set active contour model implemented in image segmentation was a geometric model and it was simultaneously proposed by Caselles et al[9] and by Malladi et al[10]. This geodesic model links the classical snakes based on energy minimization[2] and geometric active contours based on the theory of curve evolution. In order to improve the segmentation performance several authors have proposed the addition of edge and region based information sources. New active contour based models were presented by Paragios et al[11] and Zhang et al[13] for supervised segmentation integrating an energy based function with the new edge and region sources. Using a more geometric perspective Zhang et al[13] described the advantages of the model over Chan method [14] on medical images with complex backgrounds achieving robust and accurate results.

The level set theory has provided more flexibility and convenience in the implementation of active contours. Various properties of another segmentation methods, such as edges, statistics and texture, can be used depending on the implementation scheme. A segmentation method based on level that can indentify simultaneously the four cardiac chambers is evaluated in this thesis. A phase symmetry approach acting in the frequency domain in order to extract low level features of the images is of great importance for the algorithm behaviour and success [2,3].

3.2 Segmentation Method

The level set segmentation algorithm used is composed by 3 distinct phases. It begins by detecting low-level features in an image (figure 3.3b) using a Phase-based

[2] The initial closed curve adapts depending of the image forces and external constraint. It stops when the best fit between the snake and the shape of the object is found.

Symmetry Detection (PSD). This procedure is based on gradient/luminance information and on Log Gabor wavelet by finding symmetric or partial symmetric components in frequency space, allowing the enhancing of shapes in an image. The results obtained in echocardiographic images (figure 3.3b) showed to be positive in reducing the noise significantly.

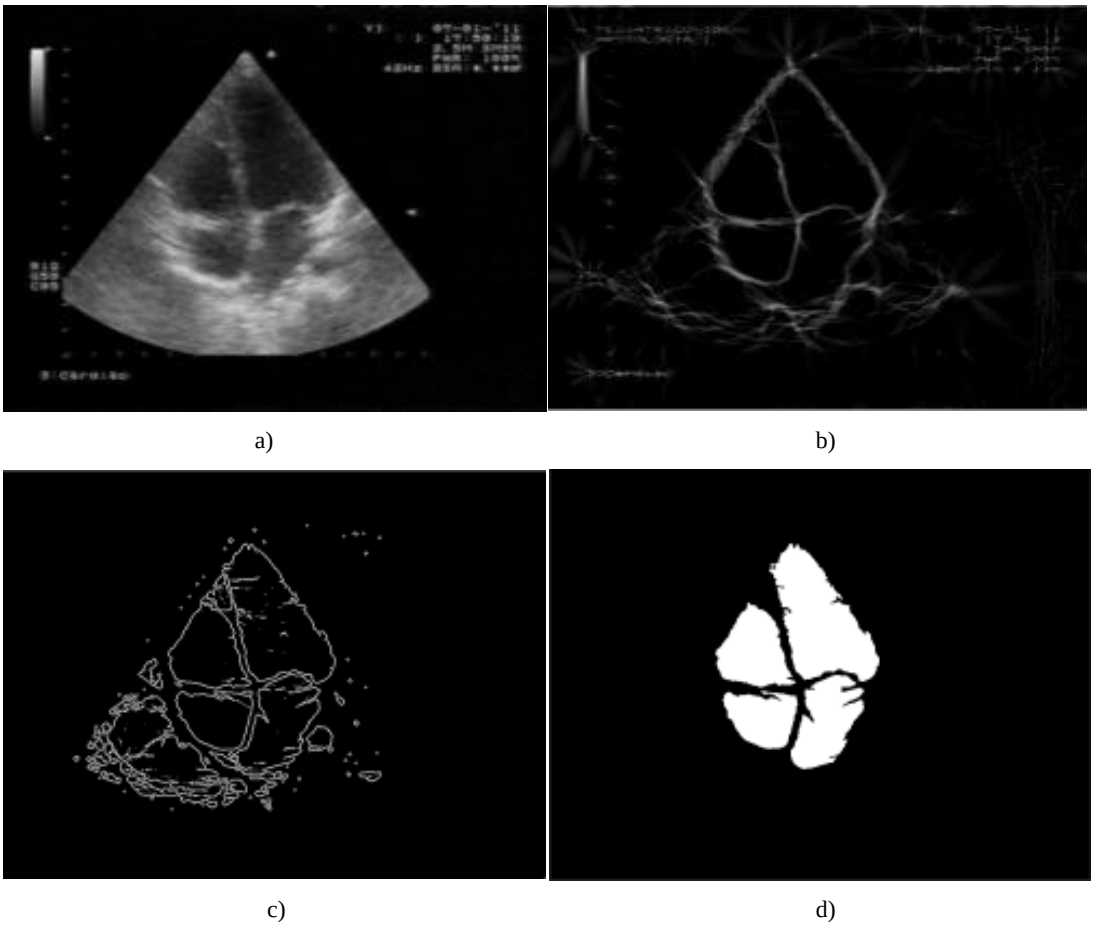

a) b)

c) d)

Figure 3.3- Echocardiographic image: (a) original Image, (b)detecting low-level features, (c) applying the segmentation method, (d) regions during post-processing.

In the second step, the main segmentation process, a modified level set is used that minimizes the function by solving the correspondent partial differential equation (PDE). By manipulating a higher dimensional function ϕ(x,t), it is possible to control a contour evolution from the beginning, based on a speed function, finding the edges of the surface.

$$\frac{\partial \phi}{\partial t} = |\nabla \phi| F \qquad (3.1)$$

$$\frac{\partial \phi}{\partial t} = |\nabla \phi| \left[div\left(\frac{\nabla \phi}{\nabla \phi}\right) + v \right] P \qquad (3.2)$$

The initial ϕ_0 function is a mask based on the Euclidian distance, where the central pixel has the biggest value and the remaining pixels decreases towards zero till they meet the image limits. Then, according to F, the function is updated at each time interval, based on shrink and expansion operations depending of the level set curvature and the stopping function P, which is represented by:

$$P = \log\left(\left|\frac{I - \varepsilon}{\gamma}\right| + 1\right) \qquad (1.3)$$

Where ε is the average intensity value of the image I and γ is the variable range of the region. This stopping function has a logarithmic variation, performs an adjustment to the regions in study and this ends by achieving convergence after few iterations. The values of the level set are: zero(at the contour), positive (inside the region) and negative (outside). Most likely more than four regions will be detected in this step.

The last step is the post-processing where all the smaller regions detected are removed, remaining the contours of the four heart cavities(figure 3.3d). Then, morphological operations dilation and closing are used to obtain smoother contours.

Chapter 4

Validation Methodology

An effective validation is critical to access the reliability of a segmentation algorithm. Only then it can be used in medical domain.

After the implementation of a segmentation algorithm it's imperative to make an evaluation to access the performance. This will be done by comparing the regions boundaries of the heart cavities detected by the segmentation algorithm with contours drawn by physicians. However there is still a problem to consider, it's impossible to find a "ground truth" for each contour. When two different physicians perform drawings of the same cavity, most likely small differences will appear between them . Even when it's the same physician drawing the same contour again after a considerable amount of time, these differences will also be noted. Regarding this, inter and intra observer comparisons were made functioning as a "golden standard" or "ground truth" in relation to automatic segmentation vs. Physician comparisons.

This chapter begins by giving an overview of used validation metrics today in this kind of evaluation. Then the contours acquisition, the validation metrics and the statistical tools are explained in detail. The main concern in each step was:

- First, reduce errors when performing the acquisition;
- Second, use different kinds of metrics;
- Third and last, obtain a graphic visualization of the comparisons making easier to perform an interpretation of the results.

4.1. State of art

For several decades, image segmentation methods have been in development, particularly in medical imaging. However systematic evaluation frameworks for these algorithms have been lagging. Sometimes investigators seem to forget that an effective evaluation is essential to present a segmentation method in medical domain[77,78].

The difficulty in establishing a "ground truth" of the segmentation and in defining performance methods and statistics have been present as the main reasons of this lag. Recently, many researchers have outlined the need of a reliable evaluation for biological images[18,79,80]. Chalana et al[18] and Hoover et al [79] argue that a reliable evaluation on large sets of common medical images is a crucial step towards establishing the clinical applicability of a segmentation method and Hoover et al[79] still claims that an objective approach is essential to avoid the inherent subjectivity of some evaluations due to human factors.

Numerous validation methodologies present some limitations such as small datasets, different datasets for different estimations of performance, not appropriate "ground truths", performance metrics poorly defined and the algorithms are only compared against other algorithms. One another limitation is related the cost in time and effort in collecting hand segmentations from physicians which normally are compared with by the algorithm segmentations[79,81]. In light of such difficulties, many researchers develop complex applications that make use of 3D visualizations of anatomical images derived from 3D and 2D segmentation methods without first evaluate them using a consistent validation strategy[82,83]. These examples exemplify the difficult in performing a comprehensive and effective evaluation in this domain.

Evaluation frameworks have been presented by several authors incorporating different performance metrics[79,80,81]. All of them agree that the use of a variety of metrics is essential to a reliable evaluation. Chalana et al[18] proposed a methodology for comparing region segmentation algorithms in medical images. The "ground truth" consisted in hand-outlined boundaries which were compared with several algorithms. Statistical tools were then used to interpret the results. Hoover et al.[79] developed a similar framework were the "ground truth" of the segmentation consisted in hand drawn contours reviewed by two human operators.

The lack of a standard framework that developers of segmentation methods could use without having to waste a large amount of time to access the performance of their methods, seems to be the primary reason of the lack of activity in evaluation. Udupa et al [84] proposed a framework similar to the one used in this thesis. The framework of this thesis consists of: 1) reliable figures of merit, 2) real image data, 3) inter/intra observer variability used as "ground truth" and 4) a software implementation incorporating the segmentation algorithm, the evaluation methods and the statistical tools.

All the work already done in this area served as inspiration to the evaluation framework used in this thesis. All the figures of merit used have been constantly referred in literature.

4.2. Contours Acquisition

To perform this step a graphical interface using Matlab R2009b[85] was developed, allowing a physician to draw the reference contours directly in the computer. The digital acquisition of reference contours minimizes the inherent error due to hand drawn contours and the corresponding digitalization, allowing a easier and more precise comparison.

4.2.1. Interface

The contour drawing begins by defining a set of points in a cavity as shown in Figure 4.1a. Then, double-clicking the right mouse button, an automatic line is generated, by a cubic spline interpolation[24] (Figure 4.1b). The line can be moved by holding a red dot to perform any necessary corrections, and finally save line x and y

coordinates. Each contour becomes associated to its image and to the physician that draw it.

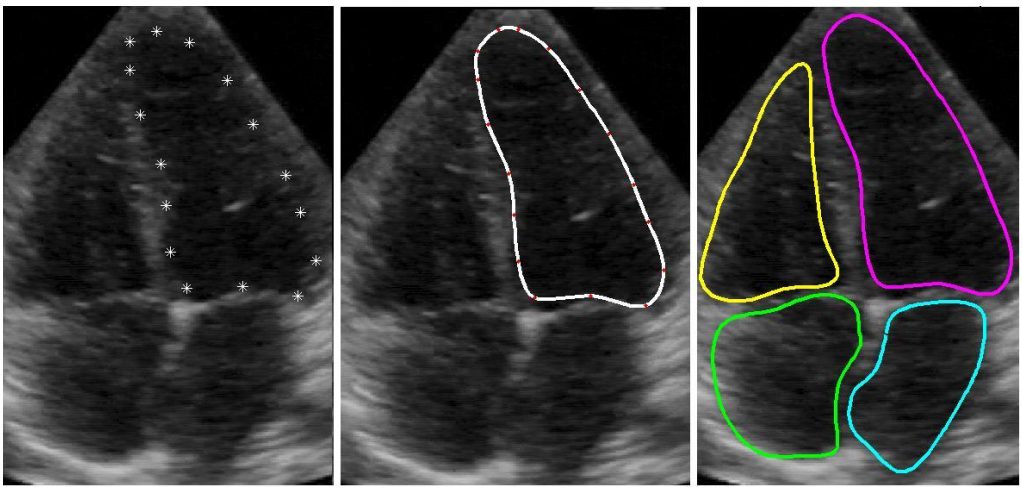

a) b) c)

Figure 4.1 - Echocardiographic image: (a) Points defined by the user (b) Cubic spline interpolation (c) Saved contours to the four cavities.

The program allows to visualize the contours individually or simultaneously and edit them if necessary at any moment. We can use various image formats and save traces of the same image under different names, for several experts as referred above.

Some images present a lot of noise and its rather difficult to visualize the four heart chambers properly, so a contrast-limited histogram equalization (CLAHE)[21] was implemented increasing the contrast of the images and accentuating the cavities boundaries. Functions for zoom and pan were also implemented.

Numerical errors are expected when it's necessary a high degree polynomial to interpolate a function from a set of points. Regarding this, Cubic Spline Interpolation uses several low degree polynomials, one for each pair of abscissae adjusting the coefficients allowing a smooth transition and maintaining the continuity if possible. This was used to interpolate the points marked by the physicians, obtaining a closed contour for each cavity. In [24,25] the Cubic Spline interpolation is explained in detail.

Contrast Limited Adaptive Histogram Equalization is a technique that improves the contrast in an image allowing sometimes a better visualization which can be very helpful in medical imaging. It differs from the ordinary histogram equalization by computing several histograms, each one corresponding to a different section of the image. Then the optimal grayscale distribution for each section is determined by

manipulating the histograms, using a previously determined transfer function, resulting in an enhanced contrast. To prevent the emergence of artificial boundaries in the output image a bilinear interpolation is used. The resulting image can be seen in Figure 4.2b.

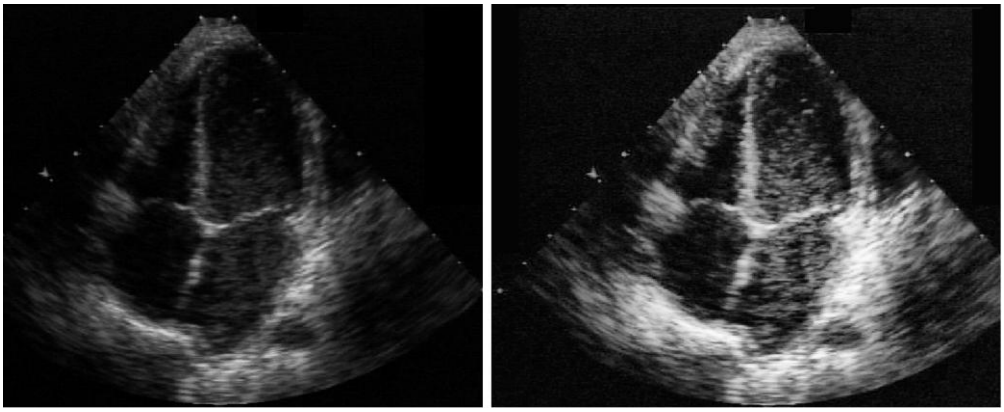

a) b)

Figure 4.2 - a)original image b) contrast enhanced image.

The major problem in this approach is that the noise present in the image is also amplified. Therefore is necessary to avoid it by limiting the contrast, mainly in homogenous areas, giving a Contrast-limited adaptive equalization[21,22,23]. Pre-defined functions were used to perform the Cubic Spline Interpolation and the Contrast Limited Histogram Equalization.

4.3.Figures of Merit

To evaluate the performance of the segmentation algorithm the contours obtained from the algorithm were compared with reference contours drawn by physicians. Several similarity metrics were used in these comparisons.

Eleven figures of merit were chosen: *Mean/Max/Larger than 5 pixels Distance[26], Pratt Function* [16,26], *Hausdorff Distance*[17, 18], *Similarity Angle, Similarity Region*[15, 16], *Accuracy, Overlap, Sensitivity* and *Specificity*[19]. They were divided in two categories: Contour and Region Based, according to their characteristics.

4.3.1. Contour Based Metrics

These group of metrics start by calculating distances between contours of the same region. To obtain the distance between corresponding points of different contours

it's necessary to define a line equidistant to both contours. In each point of this line a new perpendicular line is traced intersecting both contours. The length between them gives the distance d_i in pixels. The number of points in this line (mean contour) is equal to the number of distances (d_i) calculated. In Figure 4.4 the mean contour and a few distances d_i are presented and will be used in the first four metrics: *Mean/Max/larger than 5 pixels Distance*[26] and *Pratt Function*[16]. A different approach is used in the third metric, *Hausdorff Distance*[17,18], were there is no need of calculating a mean contour.

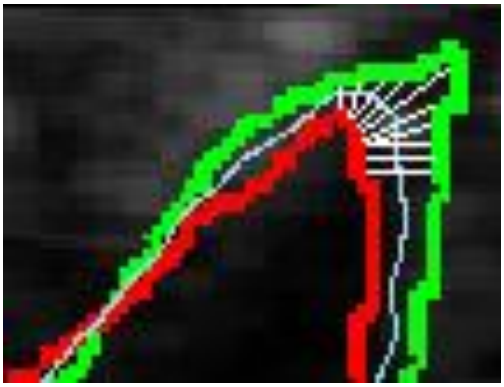

Figure 4.3 – Example of some distances d_i in white, mean contour in blue and the two contours (red and green).

4.2.1.1. Distance error

These two simple equations return the mean (4.3) and the max (4.4) d_i value obtained.

$$D_{mean} = \frac{1}{N}\sum_{i=1}^{N} d_i \tag{4.3}$$

$$D_{max} = \max(d_i) \quad , \qquad 1 \leq i \leq N \tag{4.4}$$

The variable N refers to the total number of points in a contour. The minimum possible value in both is 0, which implies total contour overlapping. There is no limit to the maximum value.

Another relation was also implemented. The function below gives the number of points in a contour were the d_i is larger than 5 pixels.

$$ND_{>5\ pixels} = \frac{1}{N}\sum_{i=1}^{N} s_i \times 100 \quad , \qquad s_i = \begin{cases} 1\ if\ d_i > 5\ pixels \\ 0\ if\ d_i \leq 5\ pixels \end{cases} \tag{4.5}$$

ND represents the number of distances and N the number of points. The binary variable s_i returns 0 if the distance is smaller than 5 pixels or 1 if it's larger. When comparing with a reference contour, for a 512x512 image, a 5 pixels distance represents 1% of error.

4.2.1.2.Pratt Function[16]

This function represents an index of similarity with a variation interval [0,1] and It's given by:

$$PF = \frac{1}{N}\sum_{i=1}^{N}\left(\frac{1}{1 + Q \times d_i^2}\right) \tag{4.6}$$

The variable N is the total number of points and Q is a normalization parameter, (1/9). This parameter corresponds to a 3 pixels distance when *PF = 0.5* which means that this metric presents bad results for large distances. This Q value has been used by several authors[15,16]. The maximum likelihood in this case occurs when *PF=1*, meaning overlap of both contours.

4.2.1.3.Hausdorff Distance[17,18]

The *Hausdorff Distance(h)* in figure 4.4, defines a distance for two given curves(A and B). When exists an overlap between them this distance is zero, otherwise it is computed the distance of each point in A, to all points in B. The smallest value is kept and for this set of distances, it is searched for the highest value.

$$h(A,B) = \underset{a \in A}{max} \ \{ \ \underset{b \in B}{min} \ \{ \ d(a,b) \ \} \ \} \tag{4.7}$$

Hausdorff Distance doesn't have a defined variation range as the other metrics, the minimal and best value is zero (contours overlapping).

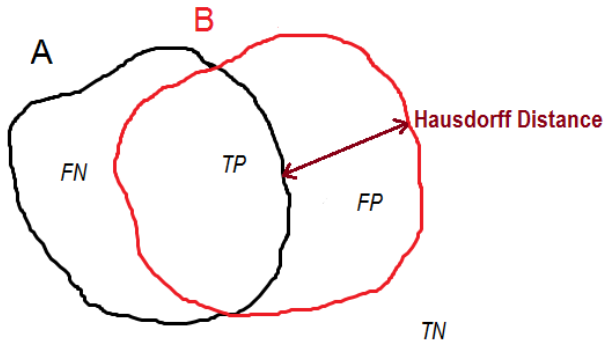

Figure 4.4- Hausdorff Distance between two contours (A and B)

4.3.2. Region Based Metrics

In this approach, the contours are filled resulting into binary images (Figure 4.5ab). It´s possible to perform a variety of operations like in Figure 4.5c were the uncommon region in both images is computed as the absolute subtraction: the pixels with the same values become 0 and with different values become 1.

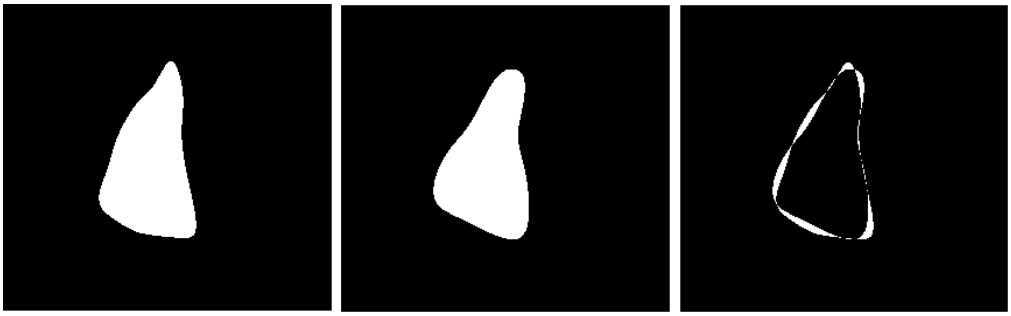

a) b) c)

Figure 4.5 - Binary image: (a) region defined by the algorithm, (b) region defined by an expert, (c) uncommon pixels of both regions.

4.2.2.1.Accuracy, Overlap , Sensitivity, Specificity

These four measures are based in the relation between two regions A and B, where A is considered has reference, and the pixels of both regions are classified as follows:

N_{TP} - *True Positive ->Pixels present in both regions*

N_{TN} - *True Negative -> Pixels absent in both regions*

N_{FP} - *False Positive ->Pixels present in B, absent in A*

N_{FN} - *False Negative ->Pixels present in A, absent in B*

N - Number of pixels.

$$Accuracy = \frac{N_{TP} + N_{TN}}{N_{TP} + N_{TN} + N_{FP} + N_{FN}} \quad (4.8)$$

$$Overlap = \frac{N_{TP}}{N_{TP} + N_{FP} + N_{FN}} \quad (4.9)$$

$$Sensitivity = \frac{N_{TP}}{N_{TP} + N_{FN}} \quad (4.10)$$

$$Specificity = \frac{N_{TN}}{N_{TN} + N_{FP}} \quad (4.11)$$

Accuracy is the ratio of correctly classified points in the ROI(Region of interest), *Overlap* gives the amount of intersection between A and B, *Sensitivity* gives the information of the actual positives that are correctly classified as positives. Specificity measures the proportion of negatives that are correctly classified as negatives. All of this metrics have a range from zero to one, were one represents the optimal correspondence and N_{FN} and N_{FP} counts zero pixels.

4.2.2.2.Similarity Angle

The *Similarity Angle* is based in the morphological similarity between two contours. Each vector ($\vec{H}$ and $\vec{I}$) is obtained transforming a 2D binary image with n×m pixels into 1D arrays with n×m pixels. They can be considered elements of a Hilbert space and using the definitions of the Euclidian inner product a similarity index was defined by:

$$SA = cos^{-1}\left(\frac{\vec{H}.\vec{I}}{\|\vec{H}\|\|\vec{I}\|}\right) \quad (4.12)$$

SA has a varies between 0º (equal contours) to 90º (completely dissimilar contours).

4.2.2.3.Similarity Region

The *Similarity Region* is a metric based in the difference between two regions(A and B), represented by:

$$SR = 2 \times \left(\frac{A \times B}{A + B}\right) \qquad (4.13)$$

SR represents the ratio between the two filled contours (A and B) and the sum of them and then its multiplied by a normalization factor. Both regions are defined by the pixels in the interior of the contour.

4.3.Statistical Evaluation

The figures of merit described earlier provide a large amount information. A reliable statistical evaluation is an important step providing solid and easy to interpret results.

In the next section the two statistical tools used, Box plots and dendrograms, are described in detail. Both of them presents the results graphically allowing an easy interpretation.

4.3.1.Box Plots

A box plots allows to represent groups of numerical data graphically trough five numerical parameters (Figure 4.6).

- **Interquartile range -** goes from the 25^{th} to the 75^{th} percentile, it´s not considered a parameter (IQR = Q3-Q1).
- **Lower quartile (Q1)** – is the median of the lower half of the data (the 25^{th} percentile). One fourth of the data goes from the minimum to the 25^{th} percentile and another fourth goes from the 25^{th} percentile to the median .
- **Median (Q2)**- the box central line (in red) is considered the second quartile.
- **Upper quartile (Q3)** – is the median of the upper half of the data (the 25^{th} percentile). One fourth of the data goes from the median to the 75^{th}

percentile and another fourth goes from the 75th percentile to the maximum .

- **Minimum (Q1 – 1.5 × IQR)** and **Maximum (Q3 + 1.5 × IQR) –** are the two smaller and higher points respectively. In the absence of outliers they are the whiskers extremes.

The outliers are considered points so dissimilar that they are not represented in the distribution. They are plotted individually using a '+' symbol. A large number of outliers can mean that the data is far from a normal distribution.

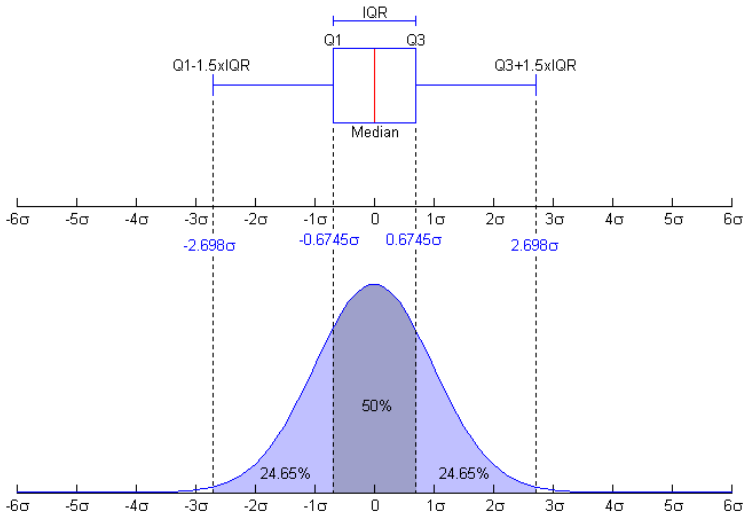

Figure 4.6- Box plot interpretation with the equivalent probability function for a normal distribution[27].

4.3.2.Dendrograms

The dendrograms are branching diagrams used to organize a set of variables according to their degree of similarity. It is produced by hierarchical clustering using a distance metric.

Hierarchical clustering works by dividing the data in several groups (called clusters). It consists from small clusters of very similar items to large clusters including more dissimilar data. There are two types of hierarchical clustering, agglomerative and divisive. Agglomerative starts by assigning a cluster for each data sample and finishes with a large cluster containing all the data samples. Divisive works in the opposite direction, starting in one large cluster and sub-dividing it in smaller ones.

Usually a graphical output known as dendrogram is generated by hierarchical clustering, representing the data set and the clusters obtained. Figure 4.7 exemplifies a dendrogram of an agglomerative hierarchical clustering.

The major characteristics of a dendrogram are represented. A **Leaf** is a sample set composed by the metrics results. This set is a matrix were the lines are the samples and columns are the variables in study. A **Node** appears when two smaller clusters are joined by connecting two **Branches**.

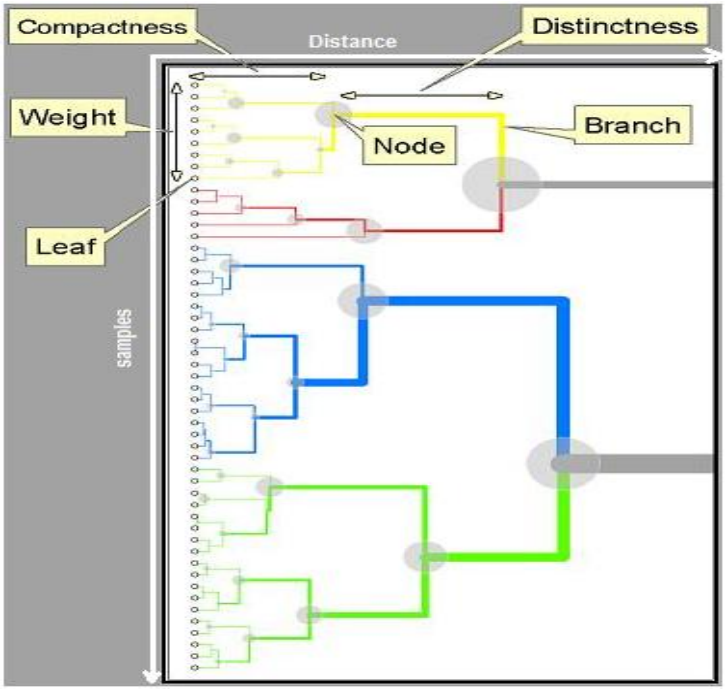

Figure 4.7 - Dendrogram example with its main characteristics[30].

Compactness and **Distinctness** are related with **Distance** between clusters (horizontal axis). For a small distance if a cluster appears, it means that the **Samples** (vertical axis) are very similar. A smaller distance implies a more compact cluster while a larger distance implies a more distinct cluster. The **Weight** represents the number of samples in a cluster. The cluster significance depends its weight, a large weight means a greater importance when interpreting the results[31,32].

Chapter 5

Validation Results

The automatic segmentation was tested against contours drawn by physicians. They were obtained using the interface explained in section 4.1. The interface proved to be very intuitive allowing a quick acquisition of contours for a large number of images. These contours were then compared with the ones obtained by the automatic segmentation using the figures of merit described in section 4.2. The statistical tools present in section 4.3 were also used to evaluate these comparisons and to infer if the automatic segmentation is similar to the contours drawn by physicians.

This is an important step to perceive if the segmentation algorithm is ready to be tested in clinical practice.

5.1 Dataset

The image database is composed by 60 images collected from two different ultrasound equipments: Acuson Sequoia 512 and Aloka SSD 2200. The images were collected from several children, approximately 10 frames from each acquisition. In Figure 5.1 two images from different equipments are presented.

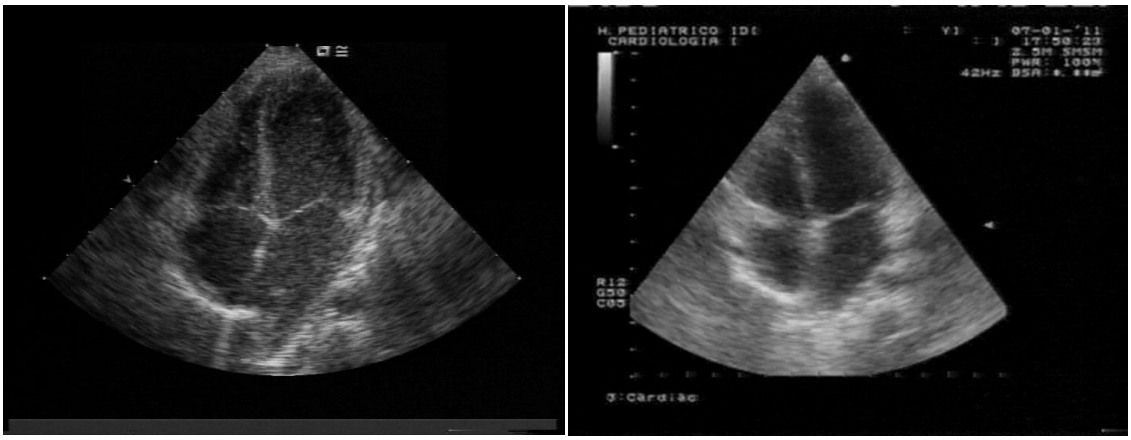

a) b)

Figure 5.1 - a) Image from Acusom Sequoia 512 b) Image from Aloka SSD 2200.

Two conditions had to be respect when the images were chosen: all of them have the four heart cavities boundaries completely visible and are in systole. They were used with the original resolution, 768×576, and in BMP format.

The dataset as 240 cardiac chambers extracted from the 60 images present in the database. Four physicians were cooperating in this study and each one performed traces for the 240 cavities twice with an interval between acquisitions of approximately 3 months. This gives a total of 480 different contours for each heart cavity.

It's still important to notice that two of the physicians were from a Central Paediatric Hospital(PH) and the others from an Central Hospital(CH). In both hospitals one of the physicians had been working for several years in the area, and the other was just starting the professional career.

5.2 Performance Assessment

The absence of a reference contour makes it impossible to perform direct comparisons. Thus it was decided to study the physicians intra and inter-observer

comparisons. This will work as a reference for the automatic segmentation vs. physician comparisons allowing to see if the variability demonstrated is similar to the reference. In order to provide more solid conclusions it was made an independent evaluation for each heart cavity and an overall evaluation using all of them at once. This allows a better understanding of the automatic segmentation behaviour and the discovery of potential errors.

In the next section the results of the comparisons are presented. The metrics will be tested independently and the differences between them will be discussed. It will also be made an hierarchical clustering for each cavity using all metrics at once.

5.3 Automatic Segmentation vs. Physicians

The 11 metrics allowed to perform an extensive evaluation. Regarding this, box plots were generated for each metric, which gives a total of 44 graphics considering the four heart chambers. Due to this large number, it was decided to perform a complete evaluation for the left ventricle, using all the metrics and for the rest only the two metrics that presented more relevant information were chosen.

Four dendrograms, one for cavity, will also be presented and analyzed. The *Euclidean Distance* was used in the hierarchical clustering. A spatial dimension is attributed to each metric. So in this case the Euclidean Distance between each comparison is computed as the comparisons were represented in an "eleven-dimension space".

Left ventricle segmentation is the most referred cavity in literature more than any other cavity [34,35] being a vital step to access the cardiac function. It is the largest heart chamber and it's were the major part of myocardial infractions occur[33]. Thus it was chosen as the most relevant cavity to perform a full statistical analysis.

It this chapter it will be used several acronyms for the contours acquisition given by:

- **A –** Segmentation Algorithm.
- **M1** – Expert Physician from PH with large years of experience;
- **M2** – Expert Physician from PH, just started his professional career;

- **M3** – Expert Physician from CH with large years of experience;
- **M4** – Expert Physician from CH, just started his professional career;
- **T1** – Contours drawn by a Physician in moment 1;
- **T2** – Contours drawn by a Physician in moment 2.

In the graphic plots, they appear like **M1T1_M2T2** which means that a comparisons was made between the two physicians using contours from different acquisitions.

5.3.1 Left Ventricle

A study with 11 figures of merit was accomplished as referred earlier. Two comparative approaches were considered: Algorithm vs. Physician (AvsM), first 8 columns, and Physician vs. Physician (MvsM) considering intra-observer (following 4 columns) and inter-observer(all the rest) variability.

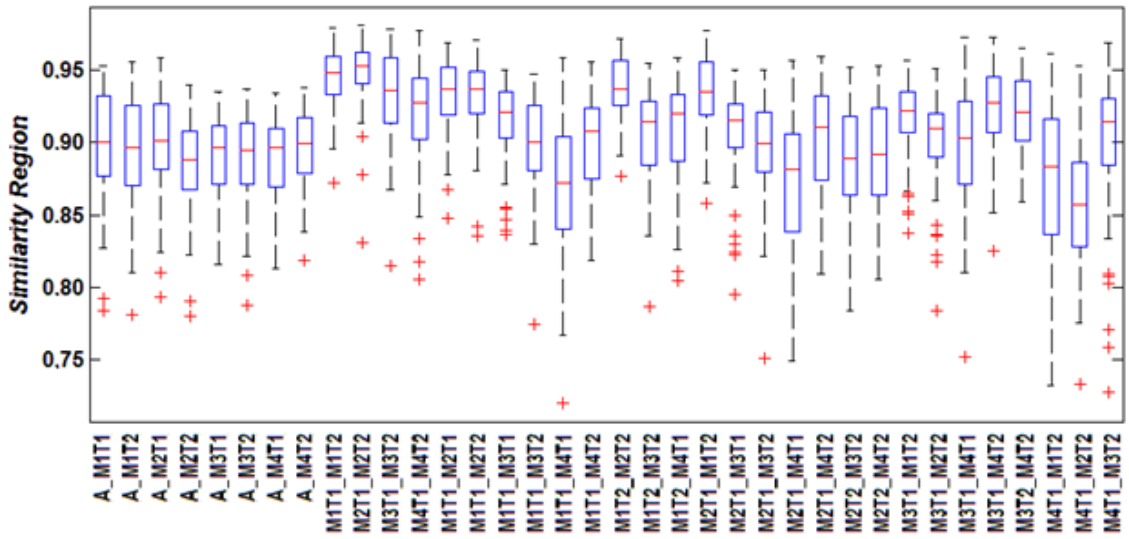

Figure 5.2 – Similarity Region Boxplots for the Left Ventricle.

Figure 5.2 shows the results using the Similarity Region. The best results appear in MvsM with medians close to 0.95. However larger differences are also denoted. While The worst median in AvsM was 0.89 and in MvsM four inferior values were found: 0.86, 0.87 and 0.88(two). Similar results appear in the 25th and 75th Percentiles. In the 25th percentile the worst value for AvsM is 0.87, while for MvsM several smaller values were found: 0.83, 0.84(three) and 0.86(two). These values imply that the worst performances were found in MvsM comparisons. They present a significant inter-observer variability (columns from 12 till the end) which. The non-uniformly

distributed box-plots imply slightly different interpretations made by some physicians when drawing a contour. AvsM comparisons do not present significant differences meaning that the algorithm behaviour is constant and possible segmentation errors can be easily predicted. All the results for the medians and quartiles obtained for the Similarity Region can be found in Appendix A, Table A.1.

Figure 5.3 presents the results for the Mean Distance. The variation is very analogous to the last metric were MvsM presented the best results.

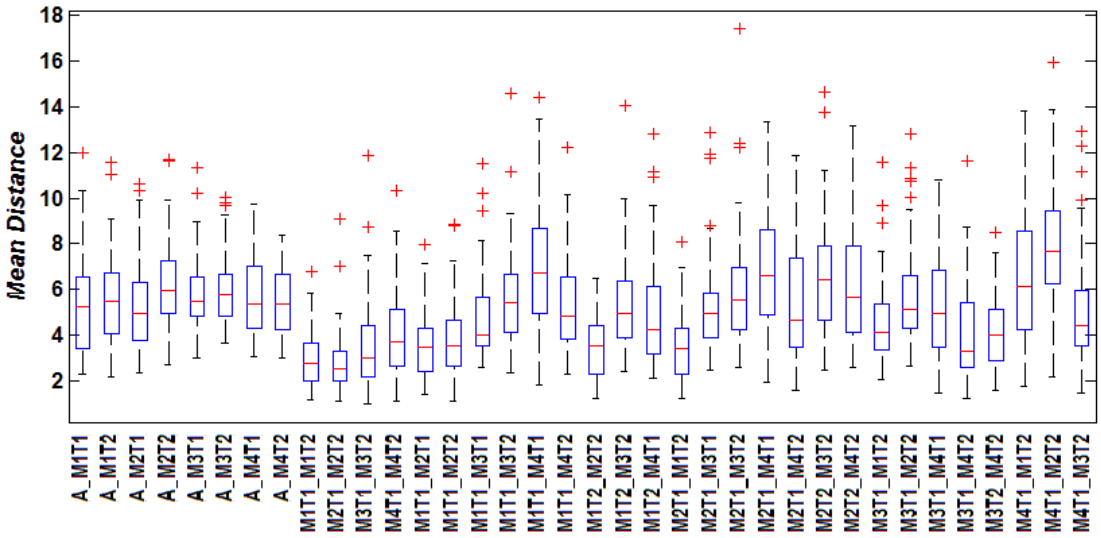

Figure 5.3 – Mean Distance Boxplots for the Left Ventricle.

The worst median for AvsM was 5.97 while for MvsM five larger values were found (6.14, 6.43, 6.59, 6.73 and 7.69). The 25th and 75th percentiles shown a similar performance and the worst values , 6.22 and 9.45, were also found in MvsM against 4.95 and 7.25 in AvsM. The conclusions are similar to the ones obtain for the Similarity Region.

The values obtained and the non-uniformity of MvsM box-plots imply that the AvsM and some MvsM (such as M1T1vsM3T2 or M2T1vsM3T2) present a similar behaviour. Once again the AvsM box-plots present an uniform distribution unlike MvsM box-plots. Complete results for the Mean Distance can be found in Appendix A, Table A.2. All the other metrics shown a similar behaviour, where the best and the worst results were also found for MvsM.

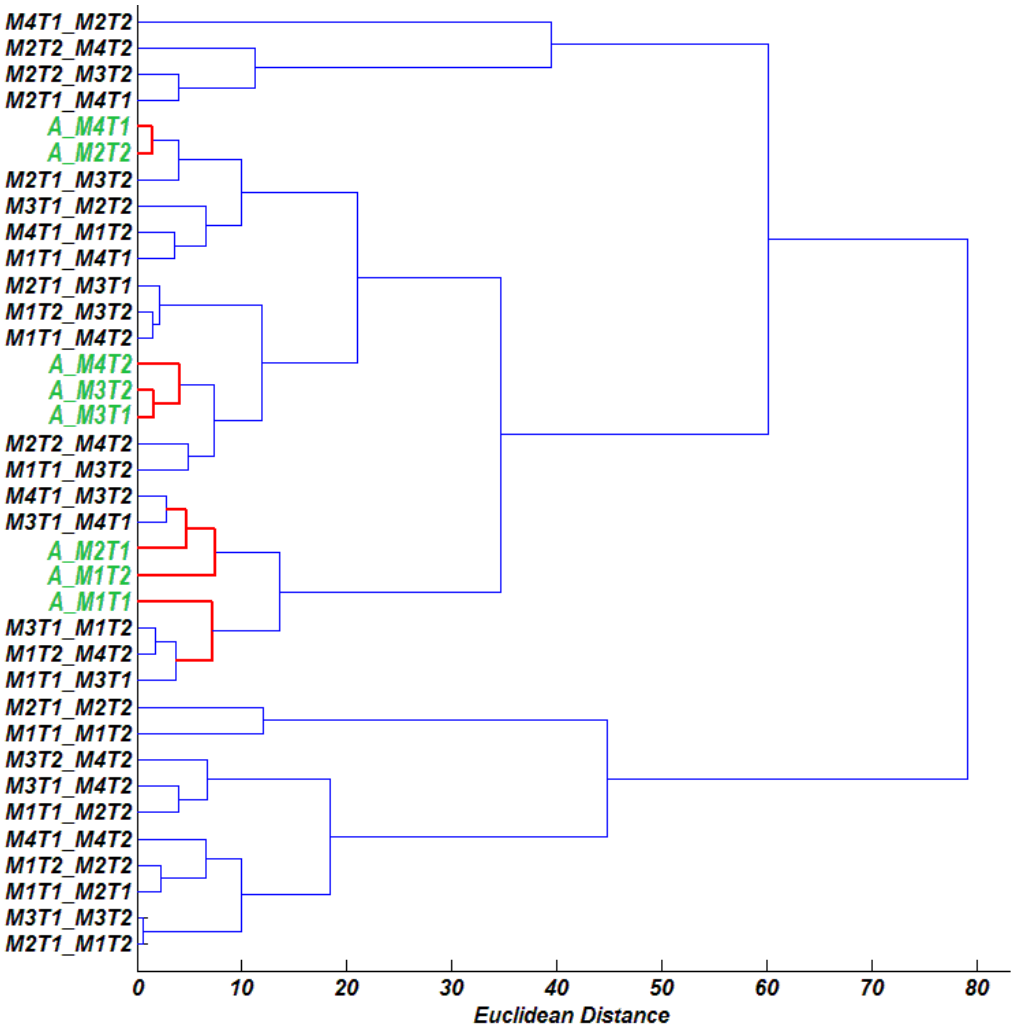

Figure 5.4 – Dendrogram Tree for the Left Ventricle using the 11 metrics.

The dendrogram plot in Figure 5.4 was obtained using all the eleven metrics. AvsM and MvsM leafs appear mixed in small clusters. For example, considering limit of 10 for the Euclidean Distance, 13 clusters are found. Some of them contain AvsM and MvsM, others just MvsM. This means that the Algorithm segmentation is closer to some Physicians than the Physicians in between. These results indicate that the algorithm presents a Physician like behaviour.

5.3.2 Right Ventricle

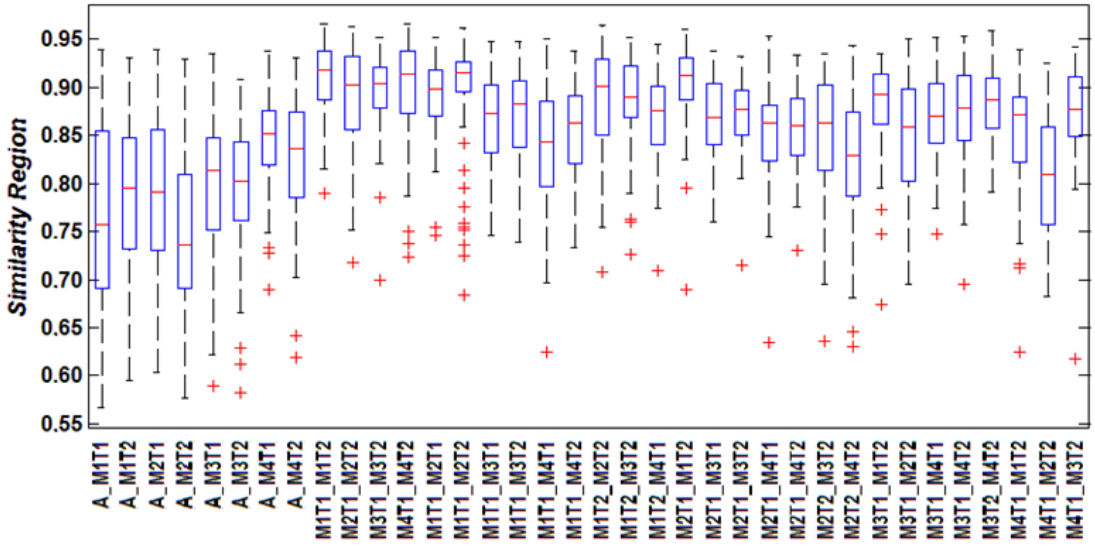

Figure 5.5 - Similarity Region Boxplots for the Right Ventricle.

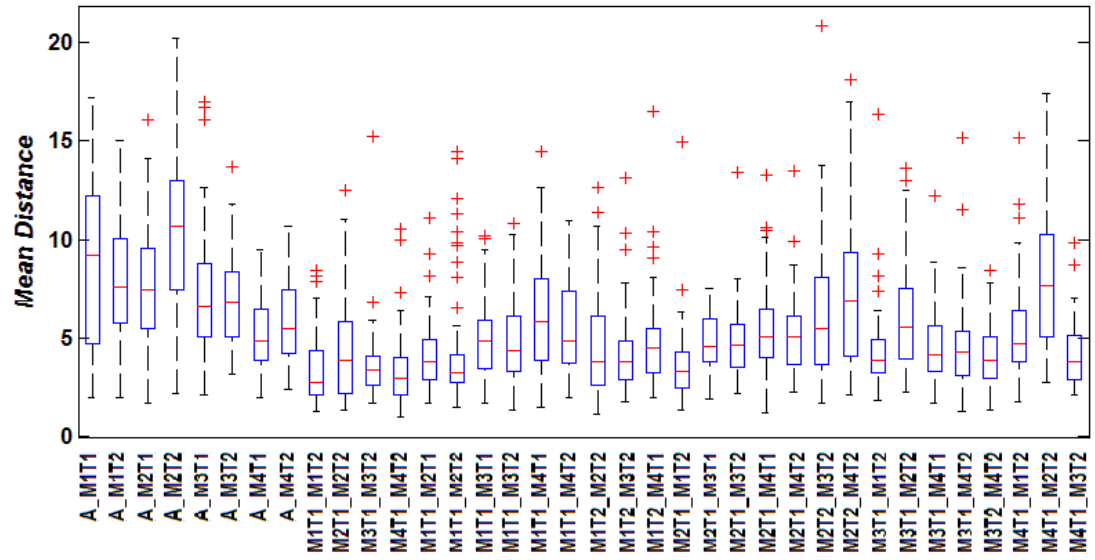

Figure 5.6 – Mean Distance Boxplots for the Right Ventricle.

Figures 5.5 and 5.6 present the Similarity Region and Mean Distance box-plots for the right ventricle. This time is visible a non-uniform distribution in AvsM comparisons. Tables 5.1 and 5.2 show the two worst results in each comparative. The worst median values in the two metrics were obtained for AvsM. A variation of 0.07 for the Similarity Region and 3.04 for the Mean Distance does not seem very significant. If two contours for the same cavity were overlapped and presented differences like these, they would be very difficult to visualize. A 3 pixels distance in a 768×576 image is rather noticeable. 75th and 25th percentile show very similar variations. The algorithm

behaviour was worse than in the left ventricle where the worst results appeared in MvsM comparisons.

Table 5.1 – Similarity Region Boxplot values for the right ventricle.

	Lower Adjacent	25th Percentile	Median	75th Percentile	Upper Adjacent
A_M1T1	0.566	0.690	0.757	0.855	0.939
A_M2T2	0.577	0.690	0.737	0.810	0.930
M2T2_M4T2	0.681	0.786	0.829	0.875	0.944
M4T1_M2T2	0.683	0.757	0.809	0.859	0.925

Table 5.2 – Mean Distance Boxplot values for the right ventricle.

	Lower Adjacent	25th Percentile	Median	75th Percentile	Upper Adjacent
A_M1T1	1.95	4.66	9.21	12.22	17.20
A_M2T2	2.14	7.45	10.70	12.96	20.25
M2T2_M4T2	2.07	4.03	6.87	9.35	16.98
M4T1_M2T2	2.71	5.07	7.66	10.28	17.40

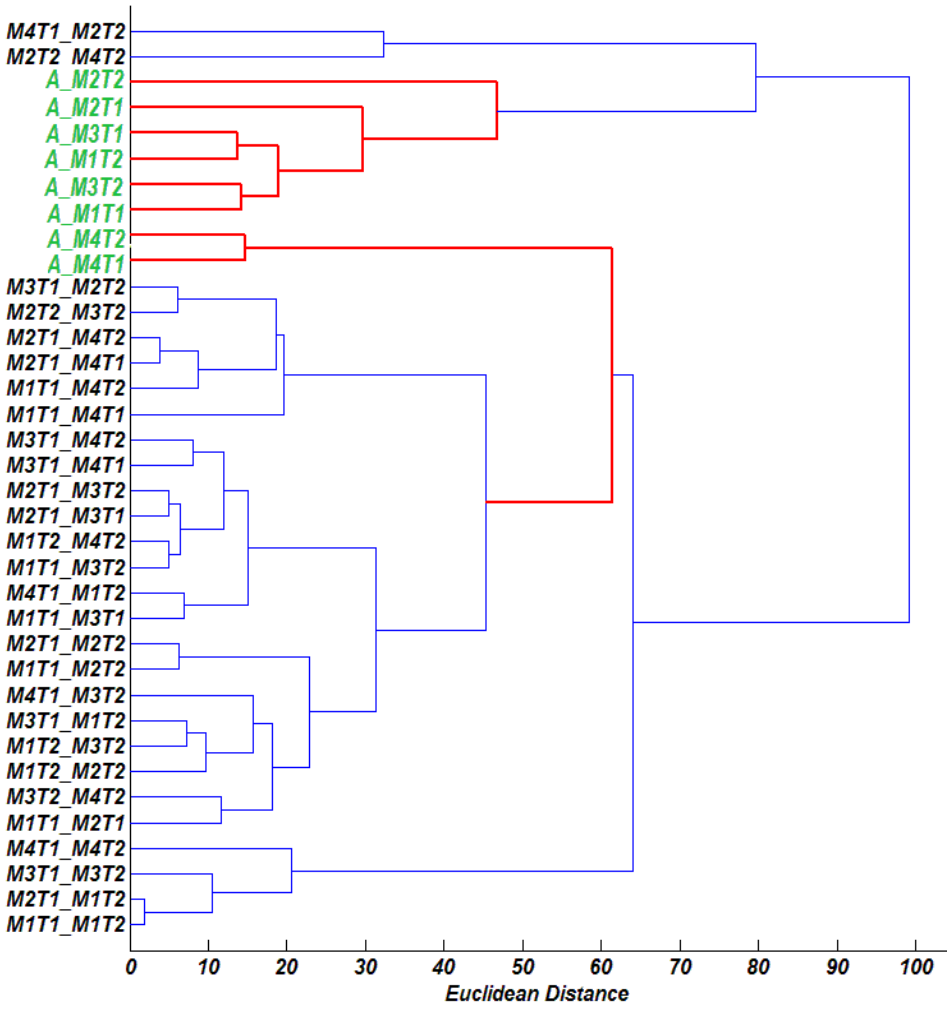

Figure 5.7 - Dendrogram Tree for the right ventricle using the 11 metrics.

The dendrogram in Figure 5.7 comes in accordance with what have been said of this cavity. In order to integrate the Algorithm comparisons with the others it's necessary to considerer an Euclidean Distance greater than 80. However some MvsM comparisons are still found in separated clusters implying a even larger dissimilarity between some Physicians comparisons. The grouping of the AvsM comparisons can also indicate that the interpretation made by the algorithm is systematically different from the major part of the physicians. An intrinsic characteristic of this cavity is probably blocking a more accurate segmentation.

5.3.3 Left Atrium

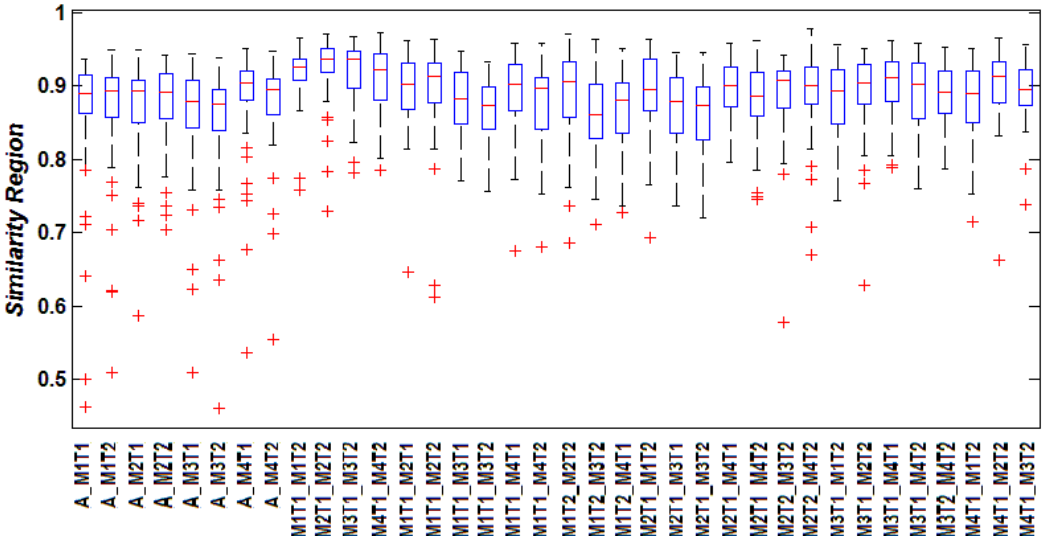

Figure 5.8 - Similarity Region Boxplots for the left atrium.

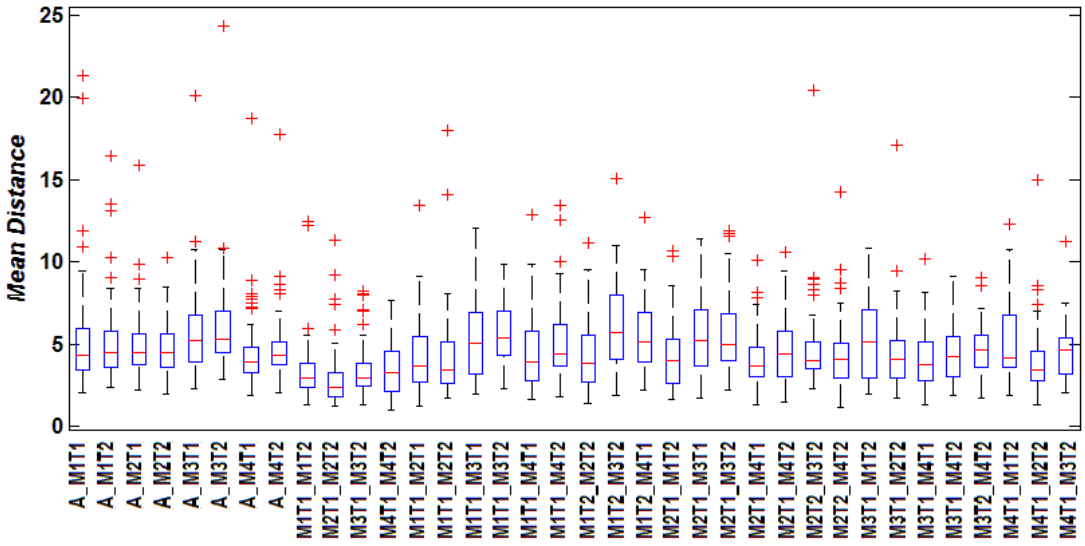

Figure 5.9 – Mean Distance Boxplots for the left atrium.

Similarity Region and Mean Distance results for this cavity, Figures 5.8 and 5.9, appear to be acceptable presenting an uniform distribution for all comparisons. AvsM and MvsM are not easily classified as belonging to different groups and the worst results were found in MvsM despite of the small differences.

Table 5.3 - Similarity Region Boxplot values for the left atrium.

	Lower Adjacent	25th Percentile	Median	75th Percentile	Upper Adjacent
A_M3T1	0.758	0.842	0.878	0.908	0.944
A_M3T2	0.758	0.838	0.876	0.896	0.938
M1T2_M3T2	0.746	0.828	0.862	0.903	0.963
M2T1_M3T2	0.721	0.826	0.874	0.898	0.945

Table 5.4 – Mean Distance Boxplot values for the left atrium.

	Lower Adjacent	25th Percentile	Median	75th Percentile	Upper Adjacent
A_M3T1	2.26	3.91	5.19	6.75	10.75
A_M3T2	2.81	4.45	5.32	6.97	10.71
M1T1_M3T2	2.30	4.28	5.41	7.03	9.85
M1T2_M3T2	1.89	4.10	5.66	7.95	10.98

Tables 5.3 and 5.4 show the worst results for AvsM and MvsM with 0.01 and 0.3 variations for each metric. These factors seem to indicate a very regular performance with small variations between all comparisons.

Figure 5.10 shows the dendrogram plot for this cavity. As in the left ventricle the two comparative approaches are mixed and distributed by several clusters, depending the considered Euclidean Distance. Using a distance of 20, four clusters are found and three of them contain AvsM and MvsM comparisons. Once more time this implicates a similar performance in all comparisons. The low Euclidean distances found (max ~40) when comparing with both ventricles (max ~80/100) seems to indicate that the visualization of this cavity is easier and it's not so dependent of the physicians experience and interpretation.

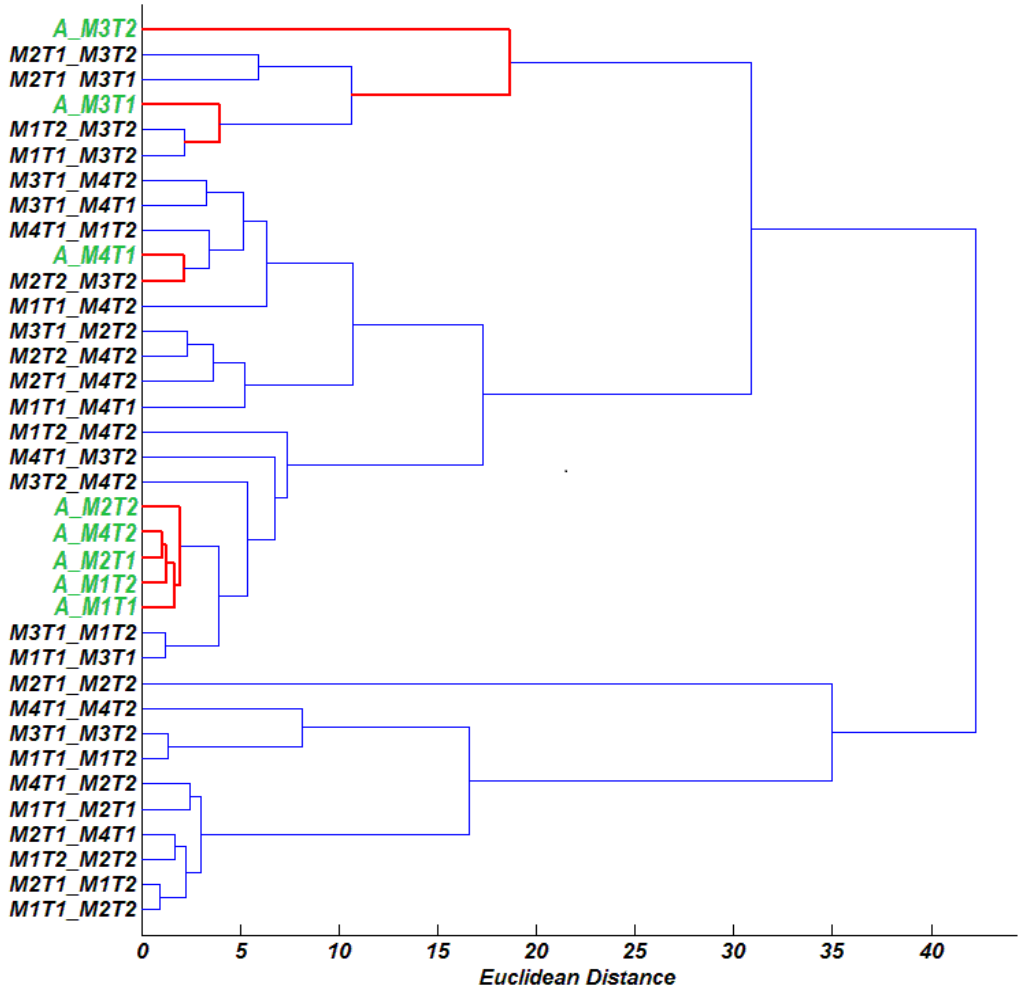

Figure 5.10 -- Dendrogram Tree for the left atrium using the 11 metrics.

5.3.4 Right Atrium

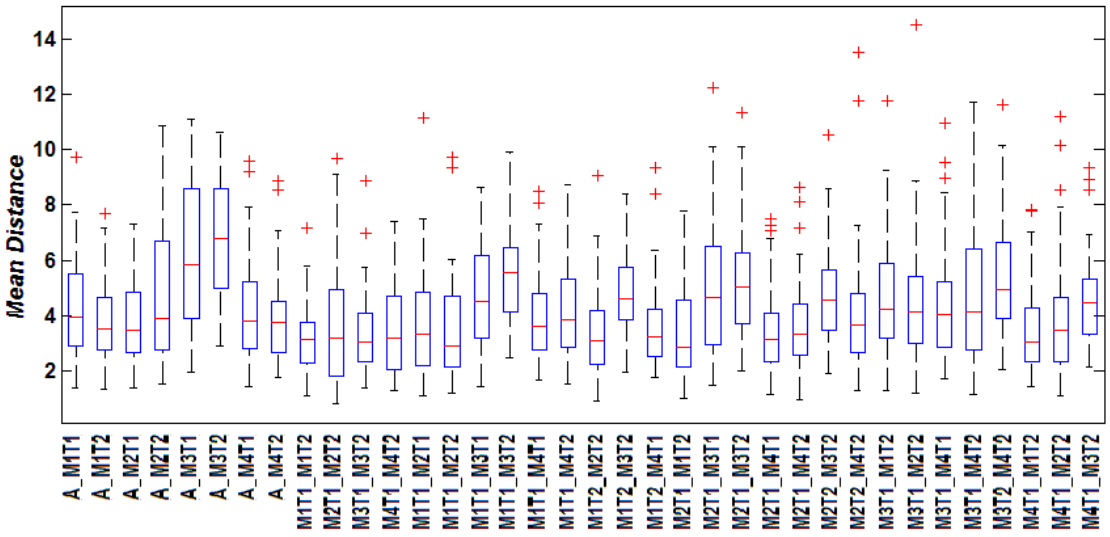

Figure 5.11 – Similarity Region Boxplots for the right atrium.

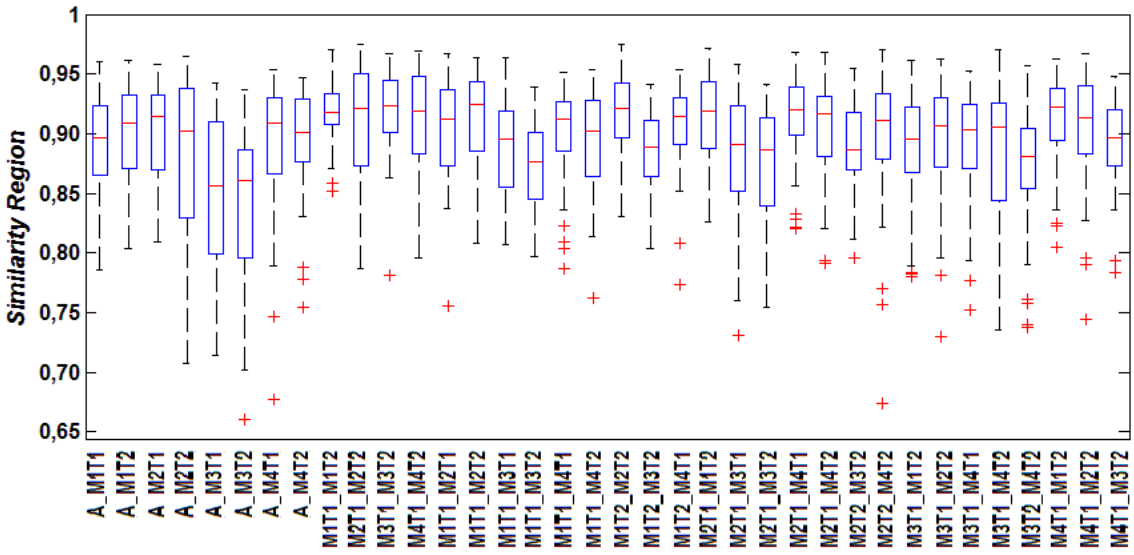

Figure 5.12 - Mean Distance Boxplots for the right atrium.

Figures 5.11 and 5.12 present the Boxplots for the right atrium. Looking to them, the two worst results are AvsM (A_M3T1 and A_M3T2) which means that this Physician contours are quite dissimilar of the ones obtain by the algorithm. However the all the others AvsM comparisons have shown a distribution similar to the one found in MvsM comparisons. This last results can be considered to present a physicians like variation.

Table 5.5 – Similarity Boxplot values for the right atrium.

	Lower Adjacent	25th Percentile	Median	75th Percentile	Upper Adjacent
A_M3T1	0.714	0.799	0.856	0.910	0.943
A_M3T2	0.701	0.796	0.860	0.886	0.936
M1T1_M3T2	0.797	0.845	0.876	0.901	0.939
M3T2_M3T2	0.791	0.854	0.881	0.905	0.957

Table 5.6 – Mean Distance Boxplot values for the right atrium.

	Lower Adjacent	25th Percentile	Median	75th Percentile	Upper Adjacent
A_M3T1	1.95	3.91	5.84	8.61	11.11
A_M3T2	2.89	4.99	6.78	8.60	10.61
M1T1_M3T2	2.48	4.12	5.57	6.44	9.92
M2T1_M3T2	1.99	3.72	5.05	6.29	10.10

Tables 5.5 and 5.6 exhibit the worst results of the two comparative approaches. Similarity Region and Mean Distance show a median variation of 0.02 and 1.21 between the inferior results of each comparative and for the $25^{th}/75^{th}$ percentile they are 0.05/0.01 and 0.87/2.16. As stated for the right ventricle the dissimilarities don't seem significant since differences even considering that this is mean distance and probably

greater distances were detected. A 1.21 pixel difference means that if the contours were represented together, the major part of the pixels would appear overlapped.

The dendrogram, figure 5.13, plot representing the hierarchical cluster presented very solid results. All the AvsM are completely mixed with the MvsM comparisons. Considering an Euclidean Distance no larger than 15, four clusters are obtained and all of them contain results of the two comparative approaches. One more time the max Euclidean distance obtained for this atrium(~35) was largely inferior to the ones obtain in both ventricles (~80/100).

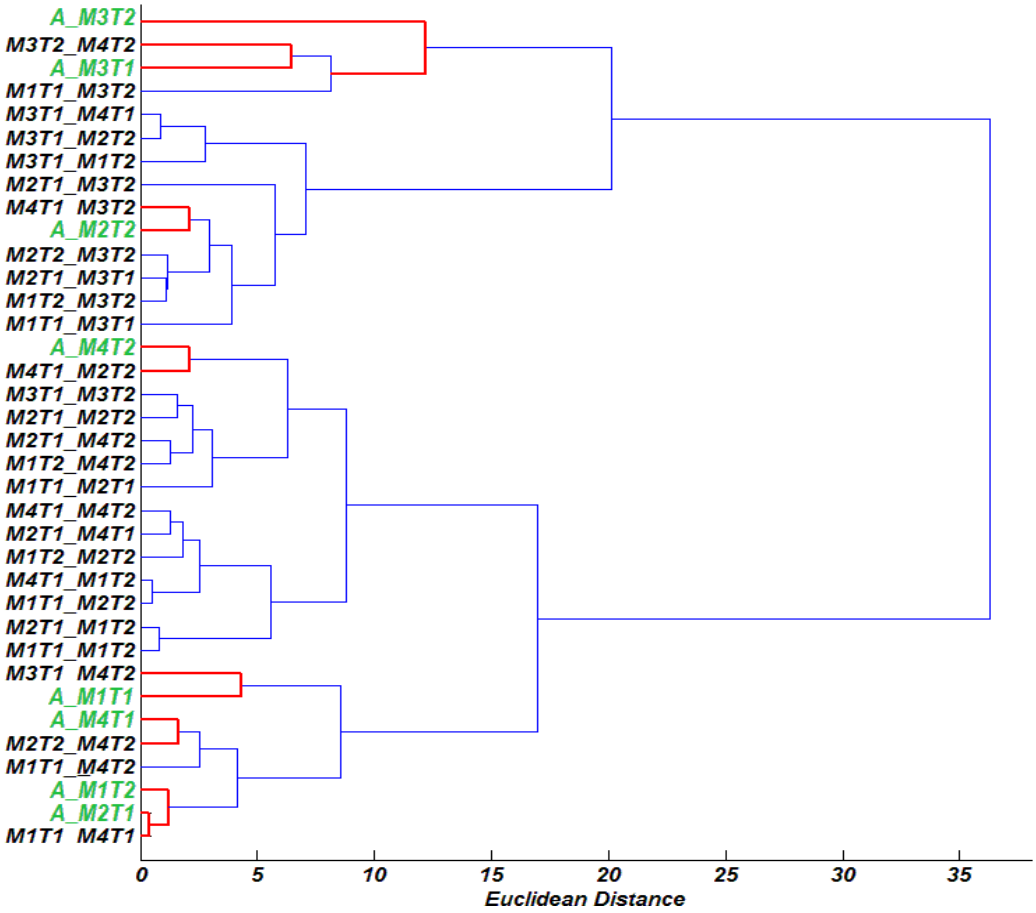

Figure 5.13 - Dendrogram Tree for the right atrium using the 11 metrics.

Everything seems to indicate that drawing a contour in an atrium is less subjective than in a ventricle. Some reasons were found to justify these conclusions. The atria represented in the echocardiographic images have smaller areas than the ventricles, so for distance metrics (like mean or Hausdorff distance) it is normal that smaller distance are also found. Another reason is the fact that in general the atria boundaries are easier to visualize, possessing a more strait interpretation. This also

influences negatively the algorithm behaviour. The large number of outliers detected in Max and Hausdorff Distance is an indicator of this fact and will be studied in the next section.

5.4 Outliers

The large number of outliers detected in some of the metrics used seems to indicate a considerable dissimilarity between contours of the same cavity. Max and Hausdorff Distance are the two best examples of this fact. In Appendix B, Figures B.5 and B.8, Algorithm comparisons present a considerable amount of outliers comparing to the ones present in MvsM comparisons.

In figure 5.14 it is depicted the worst outliers for AvsM and MvsM using the Hausdorff Distance. In fact 5.14a) shows two misjudged segmentations. In the upper-left region (right ventricle) and the down-right (left atrium). The boundaries are not clearly defined in these two regions and it's visible the presence of an artifact in the left atria which motivated the physician to draw the cavity region according to his knowledge and experience. Although These outliers also appear in lesser quantity between Physicians (Figure 5.14b)) so it's difficult sometimes to know the acceptance of these divergences.

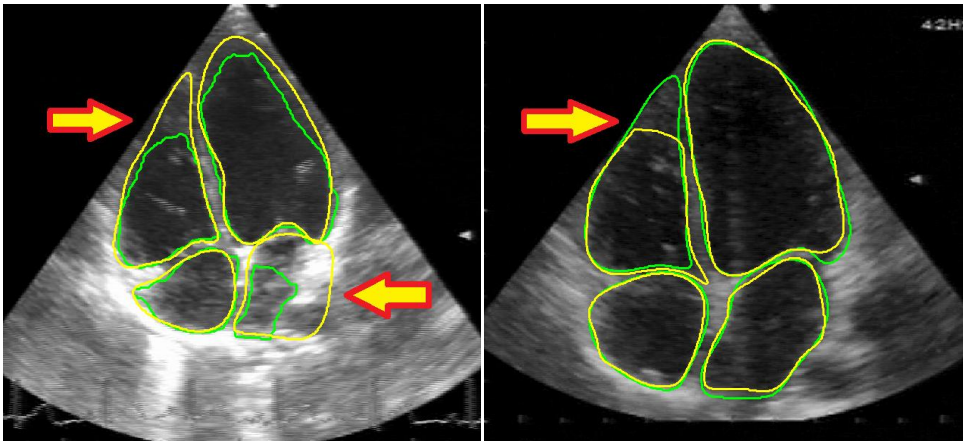

a) b)

Figure 5.14 – Contours Outliers: a) Algorithm vs. Physician (M1T1) b) Physician vs. Physician (M1T1 vs. M4T1) .

The right ventricle was the cavity that shown the larger number of contours outliers due to these circumstances which also hurt the results obtained. An acquisition

using a better equipment would improve greatly the image quality probably solving these issues.

Based on the evaluation preformed, the results discussed earlier for the median values, interquartile ranges and even the number of outliers, the automatic Algorithm seems to be reliable, performing a segmentation that when subdue to a comparative with reference drawings presents a Physician like variation. This interpretation is grounded observing all Figures from 5.2 to 5.13 where the two groups present in general analogous data distributions.

Chapter 6

Tele-Echography

An ultrasound examination requires a physician with good hand-eye coordination and capable of integrate the acquired information over time and space. These abilities are essential to mentally construct a 3D representation of the heart chamber from 2D echocardiographic images, based on the movements preformed with the ultrasound probe in order to make a diagnosis. Specialized physicians with this kind of training are not available in all healthcare centres, lacking in emergency situations when they can be of most help. A good alternative to conventional care and a way to solve some of these problems is what has been called Tele-consultation, which is a remote diagnostic system enabling to examine patients at distance. In some cases this appear to be the only possible solution to solve this problem. However the ultimate goal of this project goes beyond this, creating a 3D imaging technique using ultrasound equipment which does not require a specialized physician to perform the exam. A robotic-assisted tele-Echography setup where a robot performs an automatic acquisition has been developed. Image processing techniques has been implemented with 2D

segmentation followed by 3D reconstruction, providing 3D visualization of heart cavities and important anatomical information like cardiac areas and volumes.

An existent tele-echographic system in the Institute of Systems and Robotics (ISR) – University of Coimbra has been used to take image slices from a heart phantom. The reconstruction of these slices will be assessed by 3D visualization of heart phantom chambers.

The first part of this chapter provides an overview of medical robots, followed by the theory associated to robot forward kinematics and control, relevant to image acquisition. The last part of the chapter describes the tele-echographic system in detail.

6.1 An Overview

Nowadays, tele-echography systems can be divided into two areas: works exclusively related to the telemedicine aspect like image transmission and manipulation and works integrating the use of a robot to assist an expert operator.

MUSPAC[63] and Tele-in-vivo[64] are examples of works exclusively related to the telemedicine aspect. MUSPAC is an ultrasound medical image system that can scan patients to generate 3-D volumetric digital datasets. These datasets are then transmitted over a standard digital network to a qualified expert. Then the expert uses a virtual ultrasound probe simulating a conventional real time procedure allowing to display 2D slices from the 3D dataset simply by moving the probe interactively as in patient examinations.

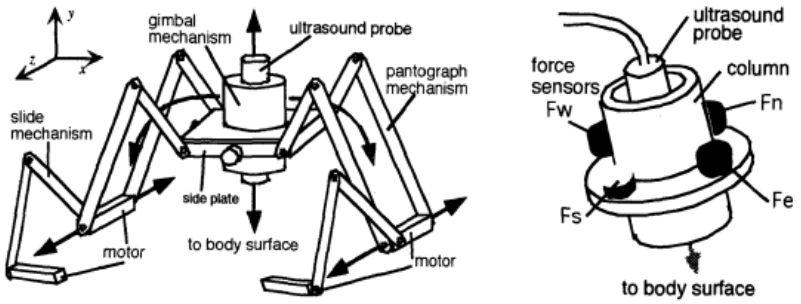

Figure 6.1 – Masuda Robot. a)basic design. b) column holding the probe with four Force sensors (Fn, Fs, Fw and Fe)[71].

Many of robot-based systems integrate conventional architectures. However medical robots belong to safety critical systems because it has a close interaction with the patient and shares its working area with medical staff. Therefore, the major part of

tele-echography robots are low-weight, compliant, safe, and portable. Some systems allow automating an echographic examination [65,66], others enable a remote examination of patients by a distant expert[67-71]. A few of them conjugate these two characteristics[65]. Several systems are being developed worldwide to remote guided procedures. They present a large variety of control schemes like shared control, force control, visual servoing and tele-operation. None of them has yet proven to be undoubtedly superior. Masuda et al[71] developed a system using slave robot (figure 6.1) with parallel arms and lying on the patient body that has no need of an assistant holding the ultrasound probe. The TER system[72], in figure 6.2, is similar to this one but possesses an original robotic architecture with force feedback. Both TER and Mitsuishi[69] systems present a sophisticated haptic device to control the robot.

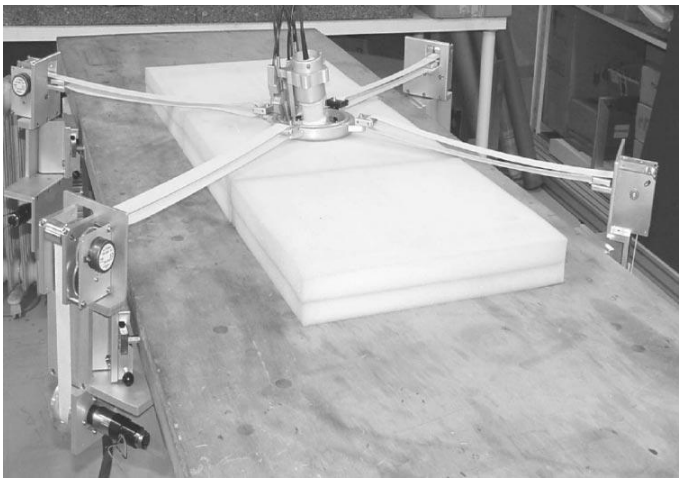

Figure 6.2 – TER system: Robot general view[72].

The Tele-echography system introduced in this work operates in a remote station with a 3D visualization environment. The robotic arm can be controlled using a computer or a haptic device. Sousa et al[76] have been working in the robot positioning and control domain using an object of study through binary computerization. The configuration developed by these authors and used in this study already allowed tele-echography between different countries.

6.2 Tele-echographic System

The tele-echographic system found at ISR can be operated remotely, requiring two separate environments: one with a webcam and the robot holding the ultrasound probe (the remote station) and the other one with a computer and a haptic device (the master station). The computer linked to the robot has 3D interactive visualization of the

ultrasound probe, showing also images of the main station through the webcam. In the master station an expert is controlling the position and orientation of the probe through the computer or the haptic device interacting with a patient (or an object of study) that is in the remote station. All the information is transmitted in real time, suffering only stochastic delays.

a) **b)**

Figure 6.3 – 7-DOF WAMTM manipulator by Barret Technology® Inc [73] and the Haptic Device Phantom desktop[75].

The main components of this system are: the robotic manipulator, the haptic device, the ultrasound equipment and a computer with all the necessary software working. The robot is a 7- DOF WAM^{TM} manipulator and it is composed by seven revolute joints (figure 6.3a). it weights ~27 kg and is torque controlled requiring dynamic and kinematic models for task space control. The Haptic device (Phantom desktop in figure 6.3b) provides force feedback and a better dexterity and it's an alternative to the keyboard/mouse. The echographic equipment(TITAN) and the transducer(model C15) is shown in Figure 6.4. The TITAN is a portable high-resolution ultrasound solution. The transducer frequency range is 2-4 MHz with 15mm bandwidth and a penetration depth of 25 cm.

a) **b)**

Figure 6.4 - TITAN^{TM} echographic equipment(a) and the C15 ultrasound transducer(b) by SonoSite® [74].

The data transmission protocol and the manipulator dynamic already can be seen in the paper written by Sousa et al[76] and it will not be explain in detail because it was not developed within the framework of this thesis.

6.3 Forward Kinematics

Kinematics is the science that studies motion (position, velocity, acceleration and all higher order derivatives) without considering the forces which cause it. A robotic manipulator as the one used in this work consists of rigid links connected rotary or revolute joints. These joints usually have position sensors allowing to measure the relative position of neighbouring links (the joint angles). The number of independent position variables that a manipulator possess can be referred as the degrees of freedom. The end effector is at the end of the manipulator. Depending of the intended application, it can incorporate a large number of devices. In order to calculate position and orientation of the manipulator, a coordinate system (or frame) is attached to the end effector and another one to the manipulator base. They are pointed as base frame and tool frame in figure 6.5.

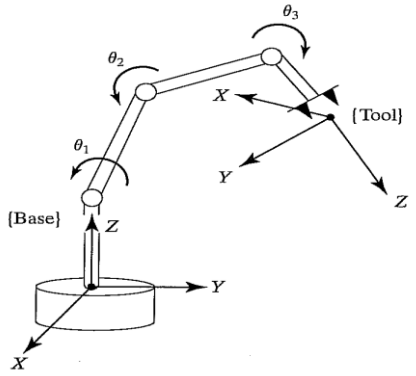

Figure 6.5 – Kinematic equations describe the tool frame relative to the base frame as a function of the joint variables[86].

Forward kinematics consists in computing the position and orientation of the end effector in relation to a static frame (as the base frame) and knowing the joint angles. Once a coordinate system is established it is possible to locate any point in space with a 3×1 position vector. As two coordinate systems are being used, the position vector must be tagged. Position vectors referenced to the base frame are referred as P_B and to the tool frame as P_T. The orientation of the tool frame is described by the unit vectors $\hat{X}_T$, $\hat{Y}_T$ and $\hat{Z}_T$. Writing them in terms of the base frame they become ${}^B_T\hat{X}$, ${}^B_T\hat{Y}$ and

${}^{B}_{T}\hat{Z}$. These three unit vector are represented together in a 3×3 matrix called rotation matrix (${}^{B}_{T}R$). The position vector and the rotation matrix are given by:

$$P_T = \begin{bmatrix} p_x \\ p_y \\ p_z \end{bmatrix} \quad ; \quad {}^{B}_{T}R = \left[{}^{B}_{T}\hat{X} \; ; \; {}^{B}_{T}\hat{Y} \; ; \; {}^{B}_{T}\hat{Z} \right] \tag{6.1}$$

When an image is acquired its position (P_T) appears referenced with respect to the tool frame (in this case the ultrasound probe frame). In that moment the robotic manipulator returns a 4×4 matrix with information of the position (point of origin) and orientation (rotation matrix) of the tool frame with respect to the base frame. The position vector that locates the origin of the tool frame is called P^{B}_{Torg} (Figure 6.6).

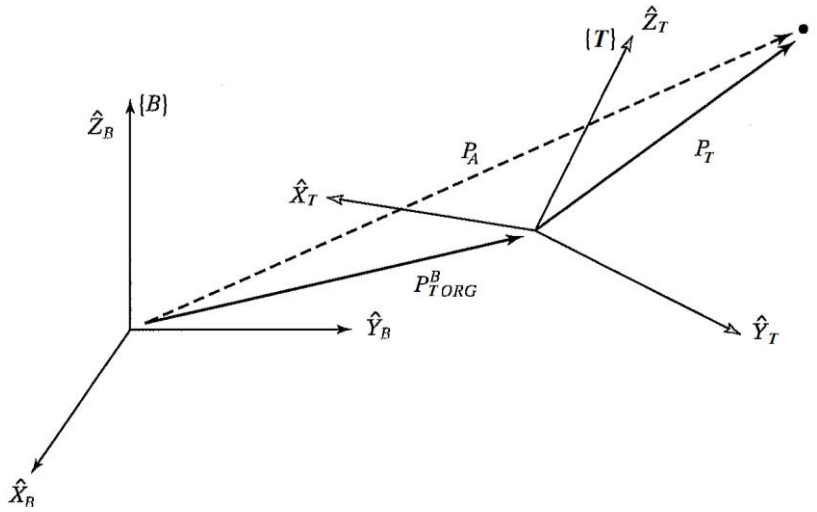

Figure 6.6 – General Transform[86].

The image position and orientation can be referenced to the base frame and it is given by:

$$\begin{bmatrix} P_B \\ 1 \end{bmatrix} = \begin{bmatrix} {}^{B}_{T}R & P^{B}_{Torg} \\ 0 \quad 0 \quad 0 & 1 \end{bmatrix} \begin{bmatrix} P_T \\ 1 \end{bmatrix} \quad \text{simplifying,} \quad P_B = {}^{B}_{T}T \; P_T \tag{6.2}$$

The 4×4 matrix ${}^{B}_{T}T$ is called homogeneous transform. It is regarded as a construction of a general transform to cast the rotation and translation into a single matrix for [86].

Chapter 7

3D Reconstruction

In medical domain, a technique able to provide a 3D visualization is sometimes mandatory. A large number of slices taken from an organ like the heart can be rather difficult to analyze requiring considerable time and storage resources. A 3D visualization can help the technician to provide a suitable diagnosis detecting abnormalities that normally would not be noticed in the 2D images.

The Level Set segmentation was used to achieve a 3D reconstruction of a heart phantom. The developed phantom simulates the heart and the surrounding environment allowing to obtain ultrasound images similar to the echocardiographic images with two or four cavities represented.

In section 7.1 the experimental setup of the heart phantom and the 2D acquisitions are described. The 3D reconstruction process is also explained in detail and the results are presented and analyzed.

7.1 Experimental Setup

The propagation velocity of sound waves in water (the human body main component) is 1484 m/s at 20º Celsius[61] which is close to the acoustic velocity in fat, myocardium and blood (1480, 1540, 1560 m/s respectively).

In order to simulate the environment present in the human body it was used a tank filled with water as illustrated in (figure 7.1a). Four balloons, also filled with water, were placed in the middle of the tank mimicking the four heart chambers (see figure 7.1b).

a) **b)**

Figure 7.1 – Experimental setup: a)Assembly simulating the heart and surrounding structures, and the robotic arm with the ultrasound probe coupled. b) four balloons simulating the cardiac chambers.

Several issues were found during the phantom assembly. First, it was necessary to isolate the tank in order to reduce the noise coming from the reflected signals on the glass walls. For that goal, styrofoam plates were used, coating the entire area of the tank, working as a wave dispersion medium. In this way the noise was reduced significantly. Another difficulty dealt with the placement of the balloons inside the tank. It was necessary to attach them to the tank walls using nylon yarns. Adhesive tape and polyurethane foam were used to help fixing the styrofoam plates and the balloons.

7.2 Slices Acquisition

The images acquisition was performed by the robot described in section 6. A simulator and a communication protocol had already been implemented for remote control and visualisation of the ultrasound probe position and orientation by using the mouse and the keyboard. The feedback provided by sensors in the robot joints returns a matrix composed by the rotation and translation vectors (the homogeneous transform). For each acquired ultrasound image, a homogeneous transform is automatically generated meaning that it has a unique 3D representation.

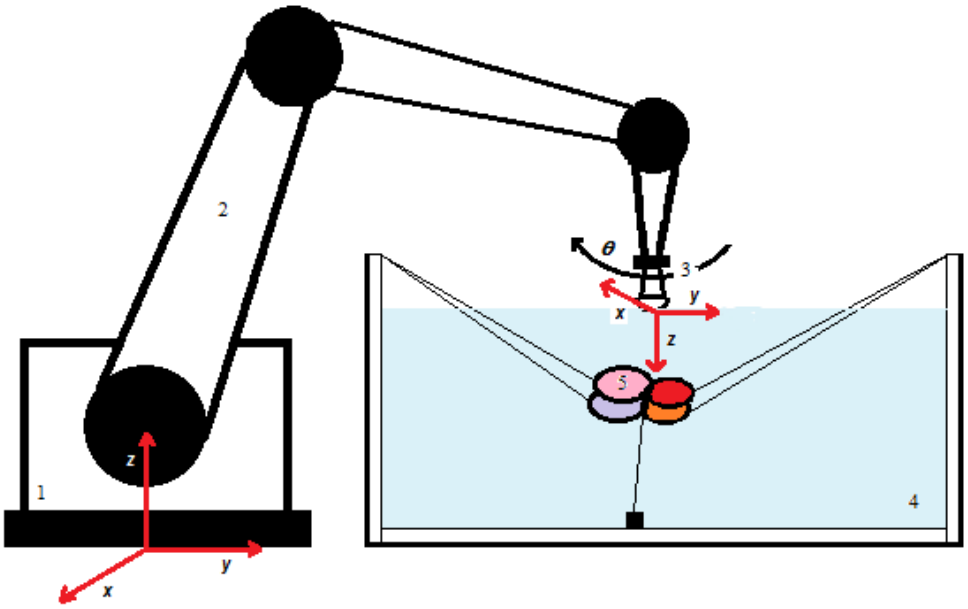

Figure 7.2 – Scheme representing the robot and the Experimental setup: 1) robot base with the reference coordinate system; 2) robotic arm; 3) ultrasound probe (rotation angle (θ) and an image coordinate system are also represented); 4) tank filled with water; 5) balloons simulating the cardiac chambers.

In figure 7.2, it is shown a schematic representation of the slices acquisition. The ultrasound probe attached to the end of the robotic arm is positioned on the top of the phantom using water as coupling. The reference coordinate system is at the robot base and the image coordinate system is also represented at the end of the probe.

Two kinds of acquisitions were made: rotational and translational. The first one consisted in executing rotation movements in z-axis of approximately 5º. In the end of each rotation a 2D frame was captured. The translational consisted in changing freely the position of the robot to capture an image. For each acquisition approximately 50

frames (phantom slices) were collected. Each frame can have two, three or four cavity views.

7.3 Data Processing

The data processing was made offline and consisted of two phases: Segmentation and 3D Reconstruction. These tasks were accomplished using Matlab 7.9.0 (R2009b).

The first phase consisted in the segmentation of the phantom slices using the Level Set algorithm, developed by Antunes et al[2] and described in section 3.2, in order to extract each cavity boundary independently. Figure 7.3 shows examples of segmented slices with 2, 3 and 4 cavities.

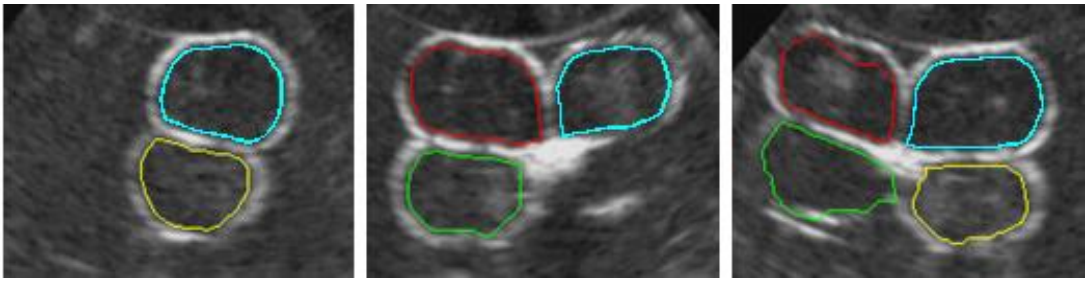

a) **b)** **c)**

Figure 7.3 – 2D slices segmented by the level set algorithm with: a)two b) three c) four cavities.

In the second phase the contours were positioned in a 3D dimensional space using the coordinates given by the homogeneous transforms. The homogeneous transforms give the position and orientation of the ultrasound probe in relation a coordinate system in the base of the robot (Figure 7.4). This coordinate system will be named base frame.

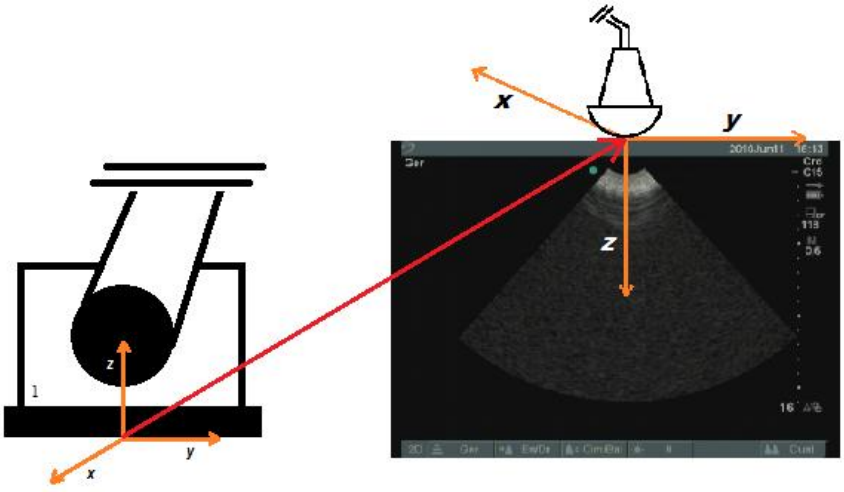

Figure 7.4 – Base and probe frame. The red arrow represents the information given by a homogeneous transform.

To perform a 3D reconstruction each contour pixels need to be referenced to the base frame. Knowing that the probe is always positioned on the top of an image, the pixels were first referenced to a coordinate system named of probe frame (Figure 7.4). Then using the correspondent homogeneous transform, each contour points(pixels) were located in respect to the base frame. After this a clustering algorithm was used to subdivide the contours in four groups corresponding to the four balloons. As each contour belongs entirely to one balloon, only the mean position of its points was used to attribute it to a region. The k-means clustering used to perform this last step will be explained next. Figure 7.5 illustrates all the steps performed from the acquisition till the reconstruction, in terms of a flow diagram.

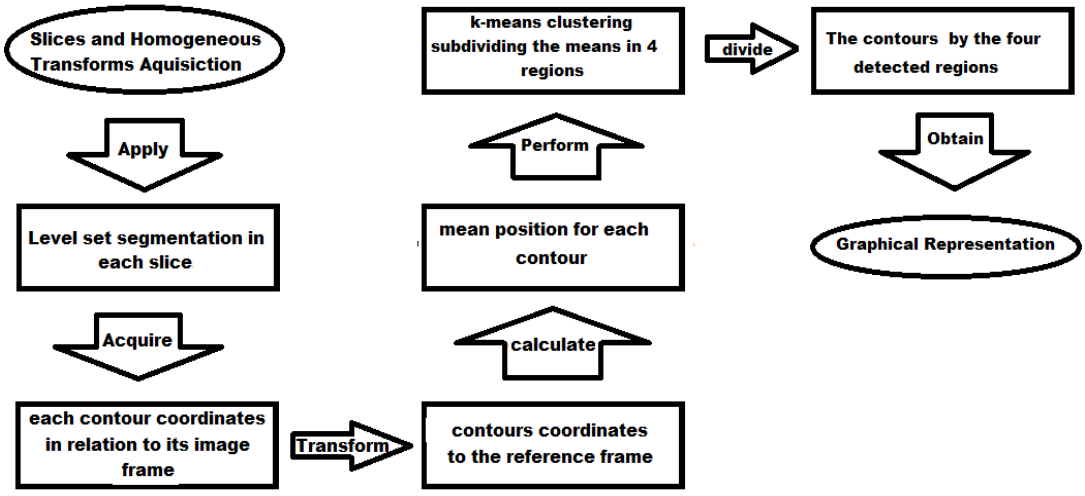

Figure 7.5 – Flow Diagram representing the steps from the acquisition till the 3D reconstruction.

Finally several graphical tools were used to represent this 3D reconstruction, namely plot3, mesh, surf and contour3. The last three ones perform interpolations thus, obtaining closed surfaces with great resemblance to the four balloons.

7.3.1 K-means Clustering

K-means clustering is a commonly used method to partition a data set in k groups. Each observation is treated as an instance (d_i) having a location in space. In the present study each contour is represented by its mean spatial position. It proceeds by:

1. Selecting k initial clusters centres (C_i).
2. Each instance d_i is assigned to the closest cluster centre C_i.
3. Each C_i is updated and becomes the mean of its constituent instances (d_i).

The steps 2 and 3 repeat until there are no further changes in the assignment of the clusters constituents/means.

It is possible to control this minimization using several input parameters like the distance metric or the maximum number of iterations. For the case in study the distance metric used was the squared Euclidean distance and the maximum number of iterations was 10.

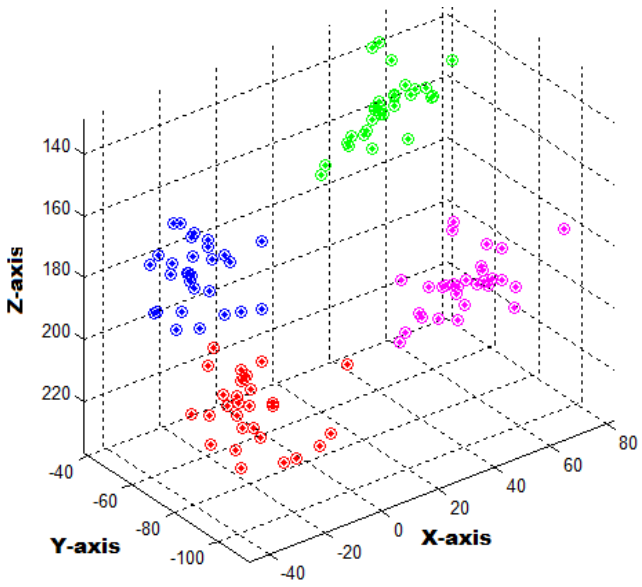

Figure 7.6 – Four Clusters obtained by k-means.

The contours mean positions of a translational acquisition are plotted in figure 7.6. The four clusters obtained by k-means appear in different colours (red blue green and magenta). A more detailed description of the k-means clustering can be found in [87].

7.3.2 Graphical Tools

The graphical tools are of simple use and understanding. A surface is defined in the z-plane above a grid in the *x-y* plane. The mesh and surf functions [62] produce wireframe surfaces that colour the lines connecting the points. The surf function displays the lines and the faces of the surfaces while the mesh function only displays the connecting lines. The contour3 compute isolines (contour lines) from the input coordinates and display them in a 3D space. Due to the similarity of the images obtained only the Contour3 plots will be analysed.

7.4 3D Results

The results of three different acquisitions were analysed: one in translation and two in rotation (in different directions). They will be referred as Rot1, Rot2 and Trans. In this evaluation the spatial positioning of the contours are analysed first. Then the interpolation results of the contour3 function are presented in order to access the reliability of the reconstruction.

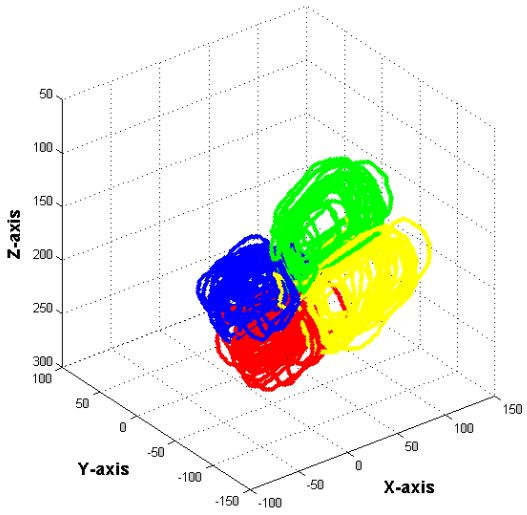

Figure 7.7 Trans Plot representing the slices of the four balloons in different colours (red, green, blue, yellow).

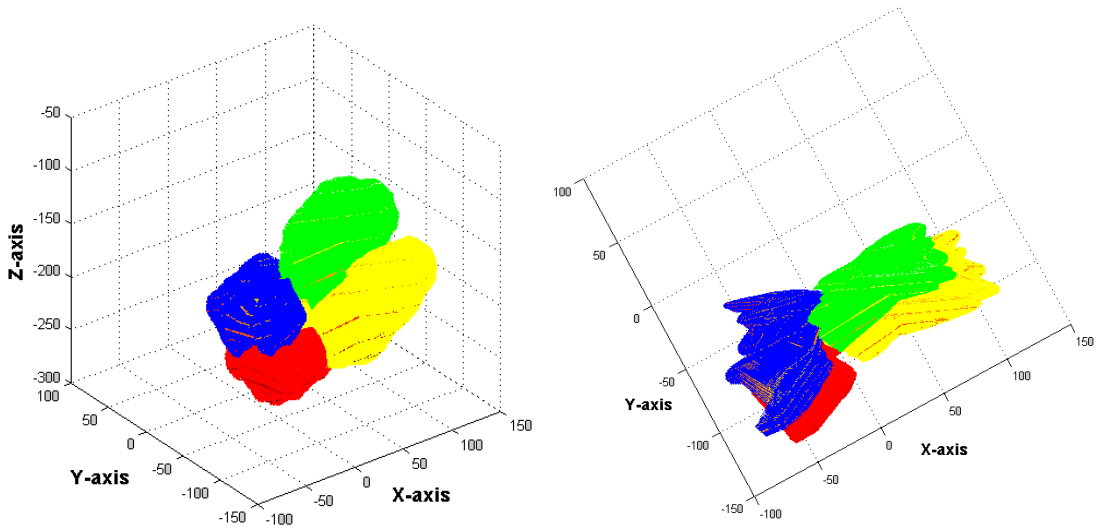

a) **b)**

Figure 7.8 – Trans contour3 plot: the four balloons are represented in different colours (red, green, blue, yellow): a) frontal view; b) top view.

The translational acquisition was made using only images that presented the four cavities. It was a primary test just to observe if it was possible to identify the four balloons. The Trans plot, in figure 7.7, presents all the contours subdivided in four

regions. The original balloons position can be visualized, however some of the contours seem to be misaligned causing discontinuities and in some cases an overlap of the four regions.

The Trans contour3 plot in Figure 7.8 presents a contour interpolation technique where the contours are represented as four closed regions. In 7.8a the area of the four regions correspond to the balloons. On the other hand, the shape is not round and smooth as it was expected. If it was not for the different colors of the four regions it would be difficult to identify them because they present some overlap. The top view in figure 7.8b shows very rough regions not resembling very much with the original balloon shapes. This is caused not only by the visible misalignments, but also by an insufficient number of slices. Cross section slices parallel to the Y-axis could improve the performance of the reconstruction giving a shape more similar to the balloons. Despite this, the considerable number of misalignments detected mainly in the blue and red regions seems to be the principal reason of the rough surfaces obtained and the great dissimilarity between this reconstruction and the original balloons. They are due to some cumulative errors from the acquisition and segmentation. Each time an image was taken the ultrasound probe had to be positioned in contact with the water in the tank. The perturbations generated could have caused slightly movements of the balloons between images. This conjugated with small segmentation errors due to the noise present in the images has probably originated the detected misalignments. There is also an error that was despised in this evaluation; the small oscillations inherent to the robotic arm positioning.

The results of Rot1 are presented in figure 7.9. The acquisition was performed with the probe positioned directly on the top of the blue balloon. The absence of some slices in figure 7.9a were compensated by the contours interpolation shown in figure 7.9b. The four regions are smooth presenting a shape similar to the balloons. The top and down views (see figure 7.9cd) corroborate those conclusions for the blue and green regions. However the red and mainly the yellow regions appear misrepresented. In the red region it is still possible to infer a balloon shape but for the yellow one the contours obtained are not enough to make the same conclusion.

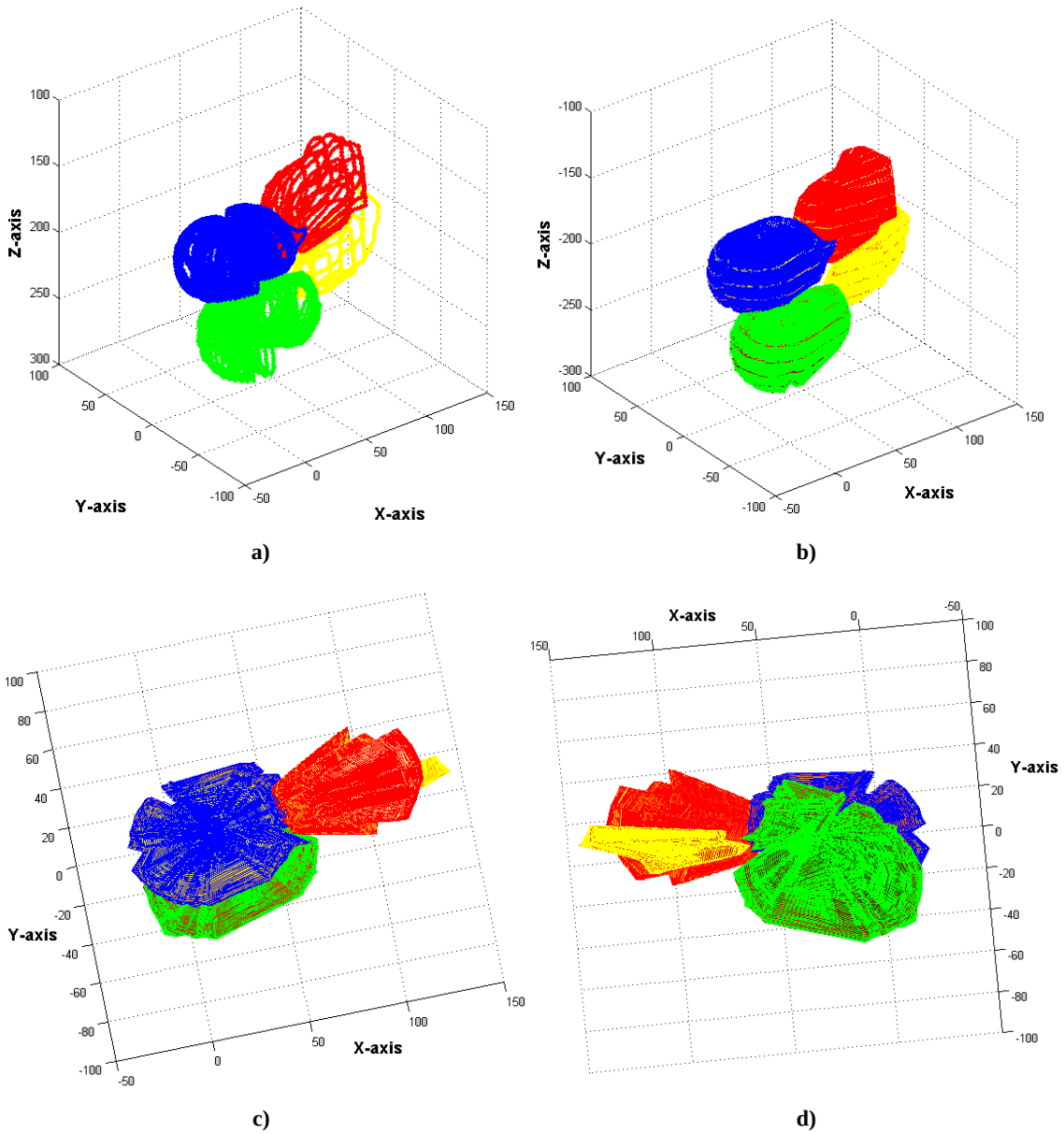

Figure 7.9 – Rot1 representing the four balloons in different colours (red, green, blue, yellow): a) Slices Plot; b)Contour3 plot; c) Top view contour3 plot; d) Down view contour3 plot.

The low number of contours acquired for this region is principally due to the noise presented in the images and the small thickness of the balloons. The balloons directly below the ultrasound probe (blue and green) were not greatly affected by these factors due to the large number of slices in comparison the peripheral ones(red and yellow). A small number of irregularities as the peak in the blue region, is visible in Figure 7.9b. They are most likely due to under or over segmentation errors. Concluding this analysis, it can be said that the blue and green regions presented satisfactory results having a shape and a volume very similar to the original balloons.

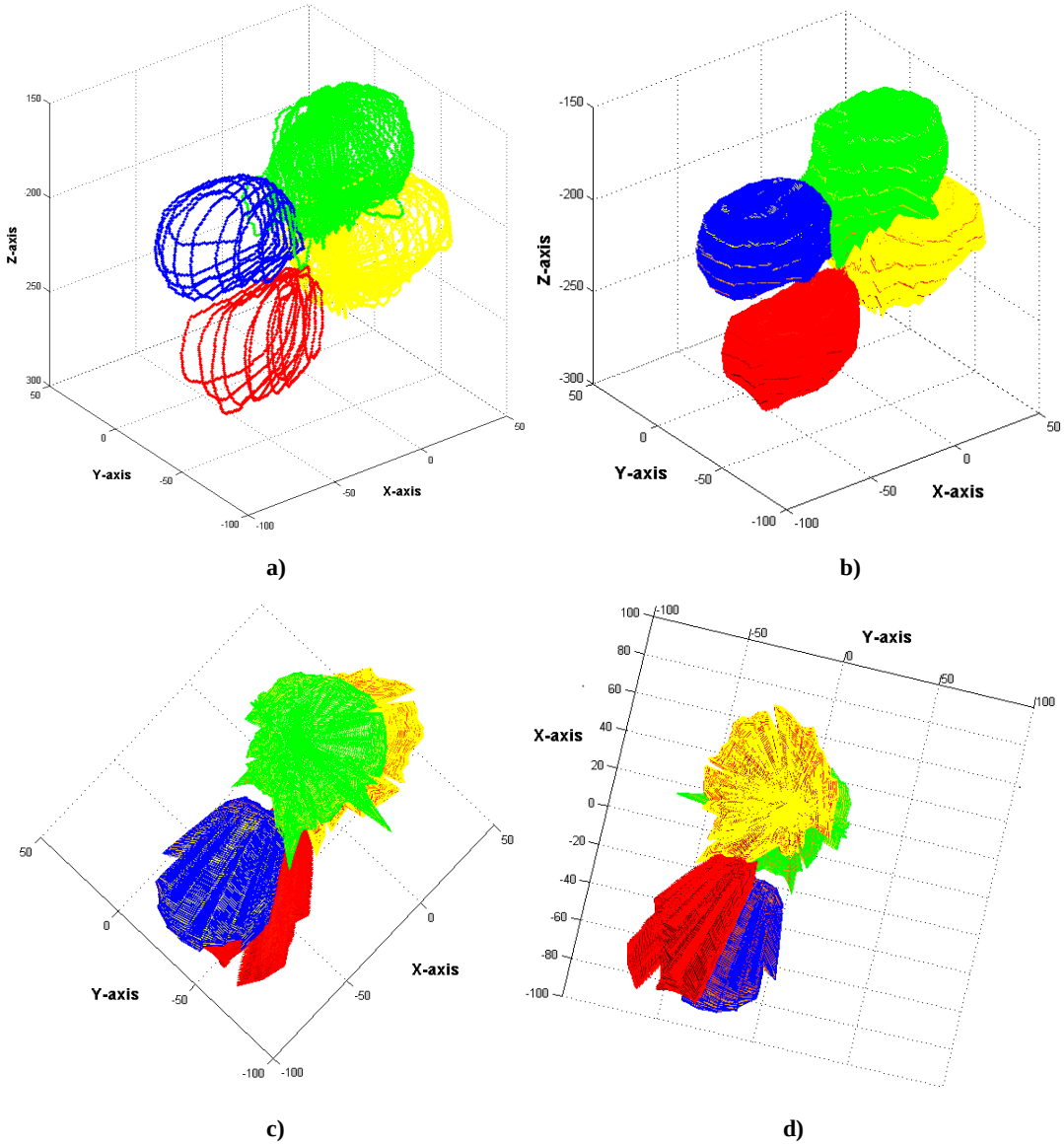

Figure 7.10 – Rot2 representing the four balloons in different colours (red, green, blue, yellow): a) Slices Plot; b) Contour3 plot; c) Top view contour3 plot; d) Down view contour3 plot.

Rot2 was performed with thicker balloons. The results are similar to the ones obtained in Rot1. All the regions appear perfectly separated and with a balloon like shape (figure 7.10b). As in Rot1 the peripheral regions in Figure 7.10cd have an insufficient number of slices to present the characteristic shape of the balloons. However it may be sufficient to access important information such as areas and volumes. Segmentation errors as the ones in the previous analysis were also detected. the peaks in the green region (Figure 7.10c) are an example of that.

It was observed that acquisitions by probe rotation presented better results than the ones by translation. This is justified by the different weight of the errors between

Rot1(2) and Trans. Just before starting Rot1(2), the robotic arm was moved in order to position the probe on the top of the balloons assembly. During the acquisition, the arm was hold still from the beginning to the end of the acquisition just rotating the end effector ~5º for each frame. The perturbations caused in the water were not visible and probably not strong enough to misplace the balloons and if the robotic arm is not moving it is not influenced by the oscillations.

7.4.1 Limitations

One of the principal goals was to development a fast method, including the segmentation and the 3D reconstruction, so that in the future it could be used online. In a laptop equipped with a Intel Core2Duo T9400 2.53GHz and 4Gb RAM the segmentation takes ~5 seconds per slice corresponding to ~4 minutes per 50 slices. The 3D reconstruction takes ~17 seconds. However the major part of the processing time is wasted interpolating the contours. The contour3 function alone takes about 8 seconds. The processing times obtained do not allow an online reconstruction but using the right equipment they could be reduced significantly.

Chapter 8

Conclusions

Cardiac boundary extraction from echocardiographic images remains an important clinical challenge. A segmentation algorithm was used for automatic contour extraction on apical long-axis four chamber view sequences of echocardiograms. The algorithm was on a representative clinical dataset composed by two hundred and forty cavities and compared the results to contours manually sketched by four clinicians. That analysis was carried out by using some figures of merit, where the performances algorithm vs. physician and physician vs. physician were of concern. It was observed that the algorithm provides results that are comparable to the inter-observer variability when the four cavities contour extraction are analyzed. Also, the algorithm performance is good when a single cavity is tested for algorithm vs. physician behaviour, and presents, in a large number of cases, superior results to the physician vs. physician achievements. The differences detected will be, most likely, due to anatomic differences

between hearts and then will be the Physician's call to take conclusions on the provided information.

This is was an indispensable step to carry on the work to the next goal, 3D heart reconstruction using 2D segmentation. A tele-echography was used to collect ultrasound images from a heart phantom. The results were not perfect and need to improve the smoothness of the cavities surfaces obtained in the 3D representation. Yet it was possible to access the shape and volume of the cavities. The reconstruction algorithm was used in an offline reconstruction. However it is quite fast and the major problem lies in the segmentation velocity. The interest in providing a reliable online heart reconstruction using echocardiography serves as great motivational factor. Thinking in how hard is to keep children quiet and lying still for a few minutes, to perform an exam like TAC or MRI is rather difficult. In addition, this is a relatively fast and economical technique. The positive results obtained with the present work, motivated the development of new approaches for the simultaneous segmentation of the four cardiac chambers, thus assisting image-guided interventions and helping the experts in the clinical diagnosis, namely in the detection of congenital heart diseases.

8.1 Future work

To finalize the evaluation of the segmentation algorithm, it would be important that the material of this thesis was used to write a paper and submit to a scientific journal in the area Ultrasound Imaging. A way to minimize the segmentation errors in large sequences of images would be to correct dropouts in one frame with previous or the following frame.

In relation to the 3D reconstruction it would be interesting apply another interpolation methods to smooth the 3D volumes. Performing larger number of acquisitions would also be important to test the reconstruction, two simultaneous rotations focused in two balloons at each time would most likely improve the results. The errors detected in the translation acquisition should be subjected to a careful analysis. Improve the phantom and make an online 3D reconstruction would be an important step before applying this technique in a real case. Here new influences will have to be considered such as the heart beat. Probably the images acquisition will have to be limited and controlled by some process like mapping the electrocardiogram in real-time.

Appendix A – Boxplots Values Left Ventricle

Table A.1 - Similarity Region Results (in bold are worst values obtained).

	Lower Adjacent	25th Percentile	Median	75th Percentile	Upper Adjacent
A_M1T1	0.828	0.877	0.900	0.932	0.953
A_M1T2	0.810	0.870	0.897	0.925	0.955
A_M2T1	0.824	0.881	0.901	0.926	0.958
A_M2T2	0.822	0.868	0.888	0.908	0.940
A_M3T1	0.816	0.871	0.897	0.911	**0.936**
A_M3T2	0.822	0.872	0.895	0.913	**0.937**
A_M4T1	0.814	0.870	0.896	0.910	**0.934**
A_M4T2	0.839	0.879	0.899	0.917	**0.938**
M1T1_M1T2	0.896	0.934	0.948	0.959	0.979
M2T1_M2T2	0.914	0.940	0.953	0.962	0.981
M3T1_M3T2	0.868	0.914	0.936	0.958	0.978
M4T1_M4T2	0.849	0.902	0.927	0.944	0.977
M1T1_M2T1	0.878	0.919	0.937	0.952	0.969
M1T1_M2T2	0.881	0.920	0.937	0.949	0.971
M1T1_M3T1	0.871	0.903	0.921	0.935	0.950
M1T1_M3T2	0.830	0.881	0.900	0.926	0.947
M1T1_M4T1	**0.767**	**0.840**	**0.873**	**0.904**	0.958
M1T1_M4T2	0.819	0.875	0.908	0.924	0.956
M1T2_M2T2	0.891	0.926	0.937	0.956	0.972
M1T2_M3T2	0.836	0.885	0.915	0.928	0.955
M1T2_M4T2	0.826	0.888	0.920	0.933	0.959
M2T1_M1T2	0.873	0.919	0.935	0.956	0.977
M2T1_M3T1	0.869	0.896	0.916	0.926	0.950
M2T1_M3T2	0.822	0.880	0.899	0.921	0.950
M2T1_M4T1	**0.749**	**0.838**	**0.881**	**0.906**	0.957
M2T1_M4T2	0.810	0.874	0.911	0.932	0.959
M2T2_M3T2	**0.785**	0.864	0.890	0.918	0.952
M2T2_M4T2	0.806	0.863	0.892	0.923	0.953
M3T1_M1T2	0.867	0.907	0.922	0.935	0.957
M3T1_M2T2	0.860	0.891	0.910	0.920	0.951
M3T1_M4T1	0.810	0.872	0.903	0.929	0.973
M3T1_M4T2	0.852	0.907	0.928	0.945	0.973
M3T2_M4T2	0.860	0.902	0.921	0.943	0.965
M4T1_M1T2	**0.733**	0.836	0.883	0.916	0.962
M4T1_M2T2	0.776	**0.828**	**0.857**	**0.887**	0.953
M4T1_M3T2	0.834	0.885	0.915	0.930	0.969

Table A.2 - Mean Distance (in bold are the worst values obtained).

	Lower Adjacent	25th Percentile	Median	75th Percentile	Upper Adjacent
A_M1T1	2.31	3.42	5.24	6.53	10.35
A_M1T2	2.16	4.08	5.47	6.73	9.09
A_M2T1	2.35	3.79	4.97	6.30	9.93
A_M2T2	2.71	**4.95**	**5.97**	**7.25**	9.94
A_M3T1	2.98	4.83	5.48	6.53	8.99
A_M3T2	**3.63**	4.86	5.79	6.64	9.24
A_M4T1	**3.04**	4.32	5.37	7.02	9.72
A_M4T2	**3.02**	4.26	5.39	6.69	8.38
M1T1_M1T2	1.15	2.00	2.75	3.63	5.83
M2T1_M2T2	1.10	2.00	2.53	3.29	4.97
M3T1_M3T2	1.02	2.20	3.02	4.40	7.48
M4T1_M4T2	1.14	2.65	3.72	5.11	8.54
M1T1_M2T1	1.41	2.38	3.50	4.32	7.15
M1T1_M2T2	1.11	2.68	3.54	4.66	7.24
M1T1_M3T1	**2.61**	3.53	3.99	5.68	8.16
M1T1_M3T2	2.34	4.12	5.44	6.65	9.34
M1T1_M4T1	1.82	**4.93**	**6.73**	**8.65**	**13.48**
M1T1_M4T2	2.31	3.81	4.86	6.55	10.15
M1T2_M2T2	1.26	2.29	3.53	4.42	6.49
M1T2_M3T2	2.43	3.89	4.93	6.38	10.00
M1T2_M4T2	2.09	3.20	4.25	6.11	9.66
M2T1_M1T2	1.23	2.28	3.39	4.28	6.95
M2T1_M3T1	2.49	3.92	4.97	5.86	8.68
M2T1_M3T2	2.56	4.26	5.56	6.98	9.79
M2T1_M4T1	1.97	**4.91**	**6.59**	**8.60**	**13.35**
M2T1_M4T2	1.58	3.45	4.67	**7.36**	11.84
M2T2_M3T2	2.44	4.66	**6.43**	**7.90**	11.20
M2T2_M4T2	2.56	4.12	5.65	**7.92**	**13.15**
M3T1_M1T2	2.07	3.36	4.11	5.39	7.66
M3T1_M2T2	**2.64**	4.33	5.11	6.61	9.48
M3T1_M4T1	1.45	3.48	4.95	6.84	10.77
M3T1_M4T2	1.25	2.59	3.29	5.44	8.75
M3T2_M4T2	1.58	2.87	3.98	5.12	7.61
M4T1_M1T2	1.78	4.22	**6.14**	**8.57**	**13.80**
M4T1_M2T2	2.17	**6.22**	**7.69**	**9.45**	**13.86**
M4T1_M3T2	1.50	3.52	4.42	5.95	9.56

Appendix B – Left Ventricle Boxplots

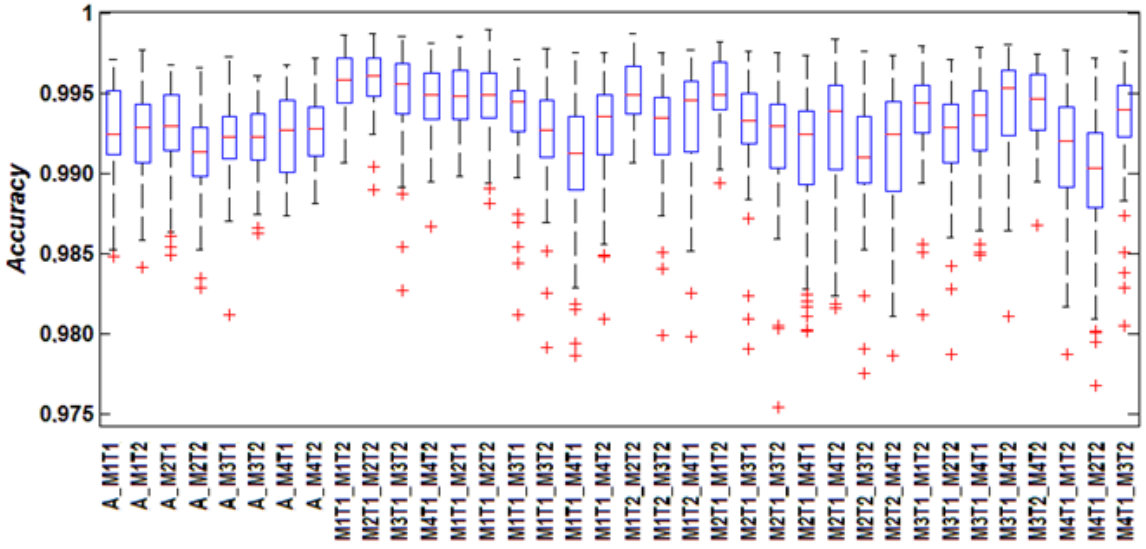

Figure B.1 – Accuracy Boxplot, Left Ventricle.

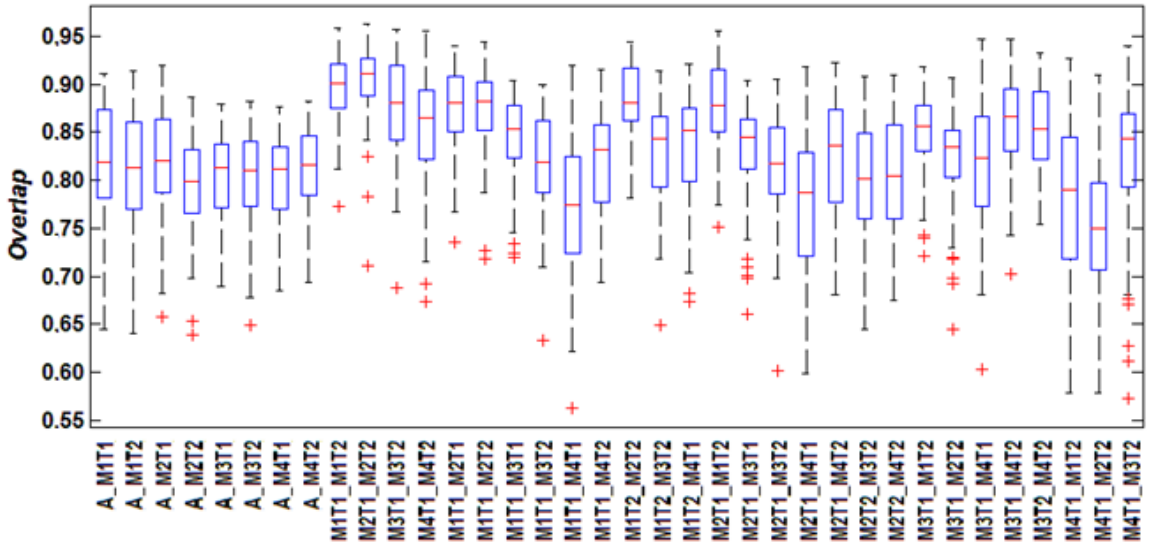

Figure B.2 – Overlap Boxplot, Left Ventricle.

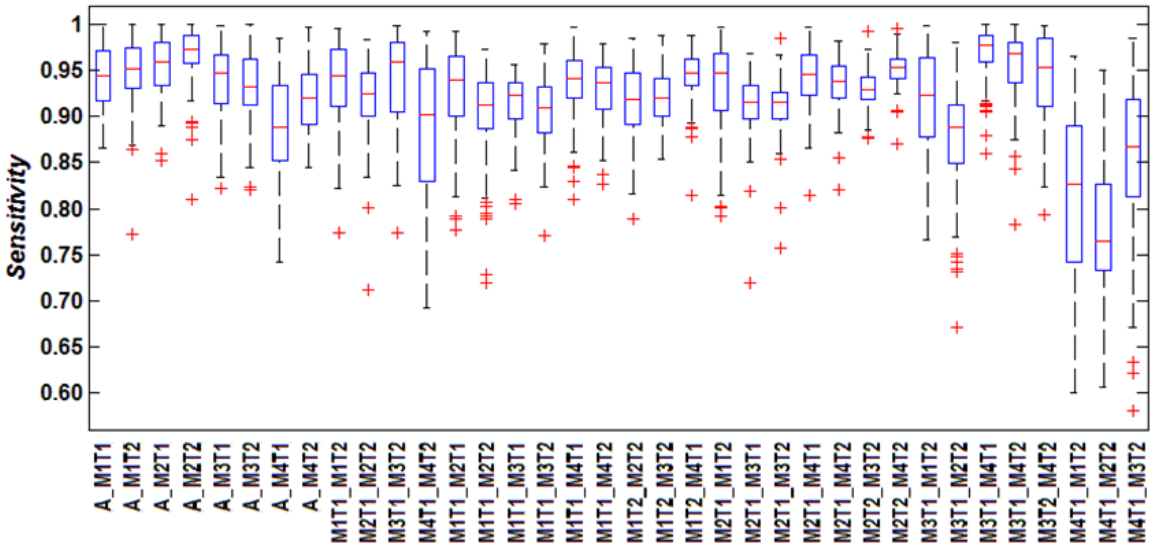

Figure B.3- Boxplot, Left Ventricle.

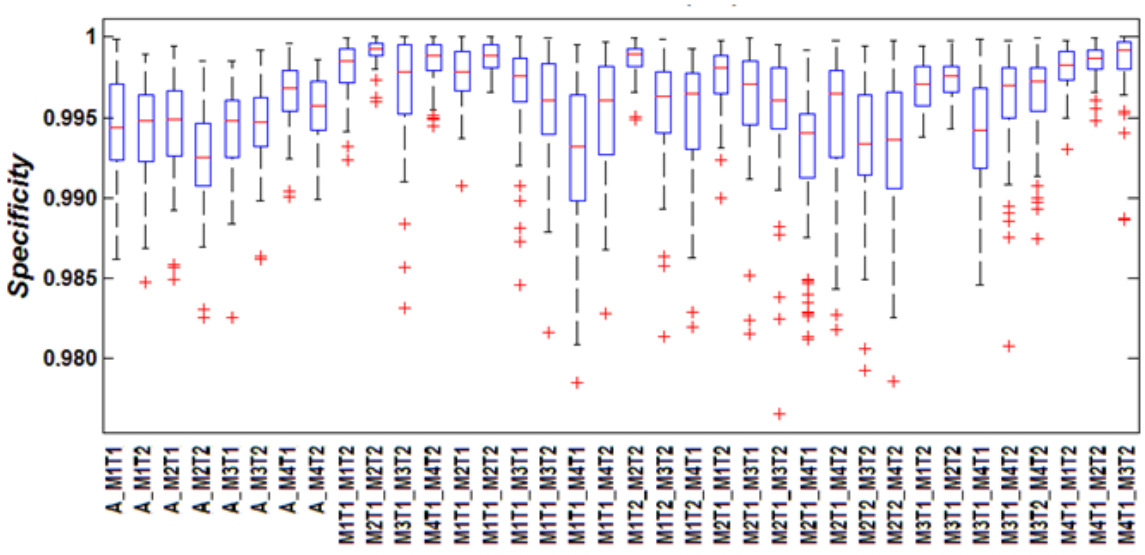

Figure B.4- Specificity Boxplot, Left Ventricle.

.

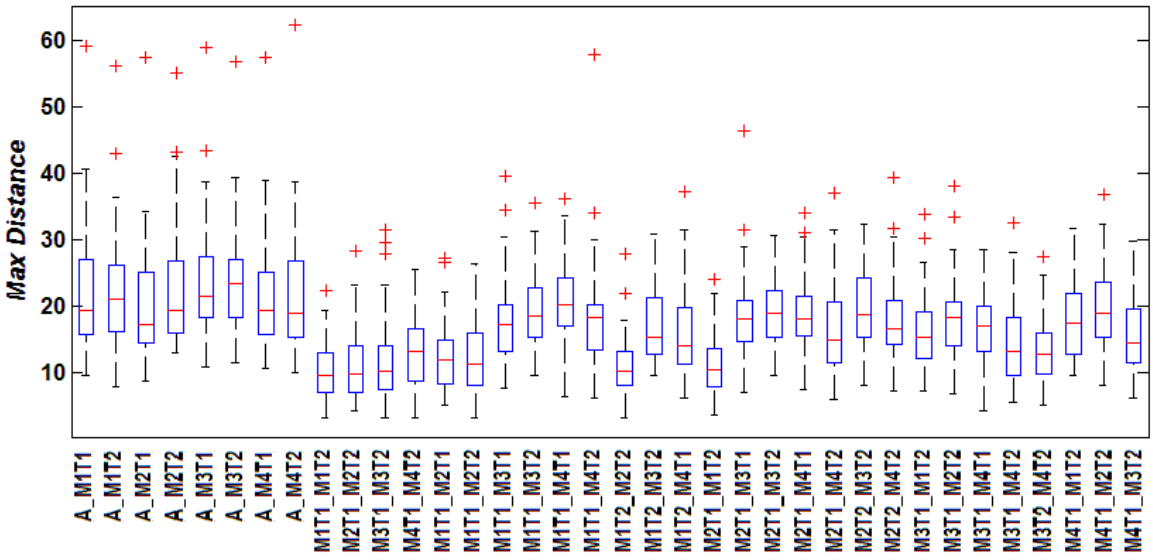

Figure B.5- Max Distance Boxplot, Left Ventricle.

Erro! Utilize o separador Base para aplicar 0 ao texto que pretende que apareça aqui.

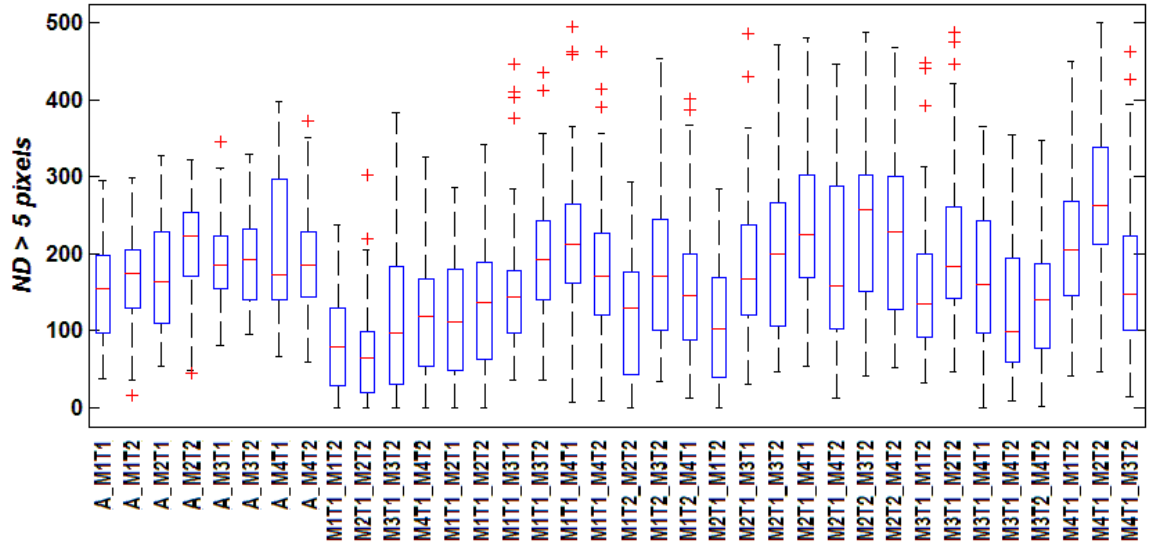

Figure B.6- ND > 5 pixels Boxplot, Left Ventricle.

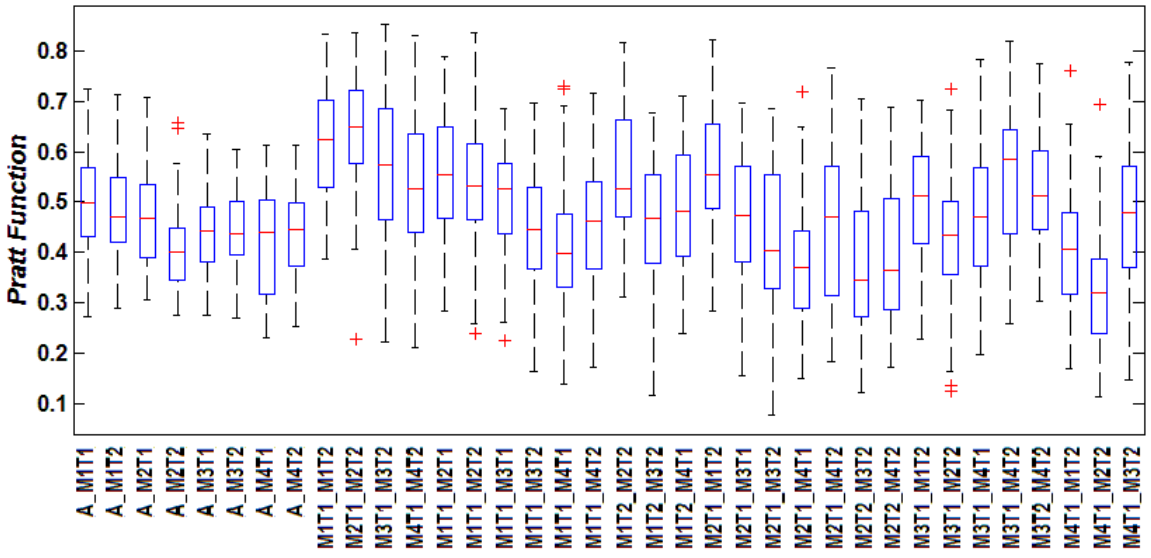

Figure B.7- Pratt Function Boxplot, Left Ventricle.

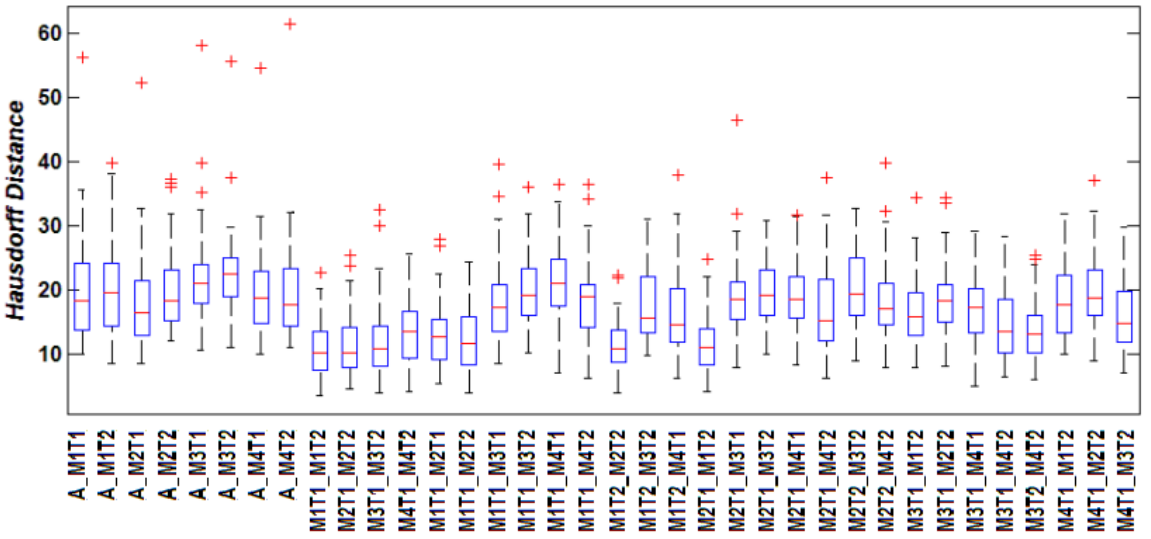

Figure B.8- Hausdorff Distance Boxplot, Left Ventricle.

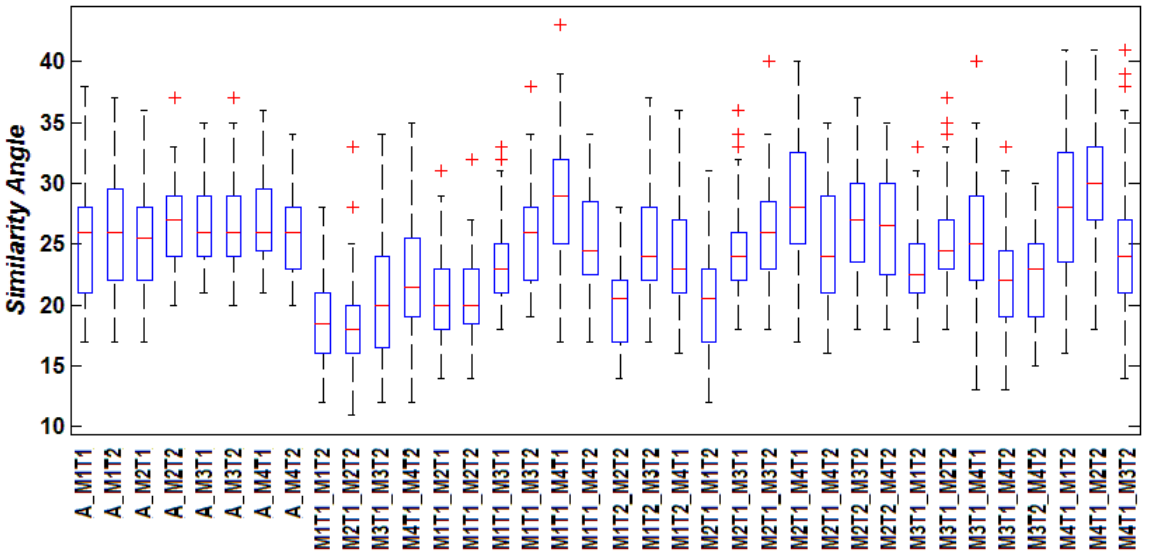

Figure B.9- Similarity Angle Boxplot, Left Ventricle.

Bibliography

1. Noble, J.A.: Ultrasound image segmentation and tissue characterization. Institution of Mechanical Engineers, part H: Journal of Engineering in Medicine, Vol. 224, London, UK 2010, pp. 307-316.

2. Antunes, S.G., Silva, J.S., Santos, J.B.: A New Level Set Based Segmentation Method for the Four Cardiac Chambers. V Iberian Conference on Information Systems and Technologies, Vol. 1, Santiago de Compostela – Spain, 2010, pp.173 – 178.

3. Antunes, S.G., Silva, J.S., Santos, J.B.: A Level Set Segmentation Method of the Four Heart Cavities in Pediatric Ultrasound Images. International Conference on Image Analysis and Recognition - Lecture Notes in Computer Science, Vol. 6112 – part II. Springer: Heidelberg, Póvoa de Varzim – Portugal, 2010, pp. 99 – 107.

4. Silva, J.S., Santos, B.S., Silva, A., et al.: A Level-Set Based Volumetric CT Segmentation Technique: A Case Study with Pulmonary Air Bubbles. International Conference on Image Analysis and Recognition - Lectures Notes in Computer Science, Vol. 3212. Springer-Verlag Berlin Heidelberg, 2004, pp. 68-75.

5. Silva, J.S., Silva, A., Santos, B.S., et al.: Detection and 3D representation of pulmonary air bubbles in HRCT volumes. SPIE Medical Imaging 2003: Physiology and Function: Methods, Systems, and Applications, Vol. 5031. SPIE - The International Society for Optical Engeneering, U.S.A., 2003, pp. 430-439.

6. Silva, J.S., Cancela, J., Teixeira, L.: Intra-Patient Registration Methods for Thoracic CT Exams. Second International Conference on Bio-inspired System and Signal Processing, Porto – Portugal, 2009, pp. 285-290.

7. Ferreira, A., Morgado, A.M., Silva, J.S.: Automatic segmentation of corneal nerves structures using region growing approach. Proceedings of CISTI 2010, Vol. 2, Spain, 2010, pp. 269-270.

8. Kass M., Witkin A., Terzopoulos D.: Snakes: Active contour models. International Journal of Computer Vision, 1988, vol.1, pp. 321-331.

9. Caselles, V., Kimmel, R., Sapiro, G.: Geodesic Active Contours. International Journal of Computer Vision, 1997, vol.22, pp. 61–79.

10. Malladi R., Sethian J.A., Vemuri B.C.: Shape Modeling with Front Propagation: A Level Set Approach. IEEE Transactions on Pattern Analysis and Machine Intelligence, 1995, vol.17, pp. 158-175.

11. Paragios N., Deriche R.: Geodesic active regions: A new framework to deal with frame partition problems in computer vision. Journal of Visual Communication and Image Representation, 2002, vol.13, pp. 249–268.

12. Paragios N.: Variational Methods and Partial Differential Equations in Cardiac Image Analysis. 2004 IEEE International Symposium on Biomedical Imaging: From Nano to Macro, Arlington, USA, 2004, pp. 17-20.

13. Zhang Y. et al.: Medical Image Segmentation Using New Hybrid Level-Set Method. Fifth International Conference Biomedical Visualization: Information Visualization in Medical and Biomedical Informatics. IEEE Computer Society, London, UK, 2008, pp. 71-76.

14. Chan T.F., Vese L.A.: Active Contours Without Edges. IEEE Transactions on Image Processing, 2001, vol.10, pp. 266-277.

15. Santos B.S., Ferreira C., Silva J.S., et al.: Quantitative Evaluation of a Pulmonary Contour Segmentation Algorithm in X-ray Computed Tomography Images. Academic Radiology, 2004, vol.11, pp. 868-878.

16. Silva A., Silva J.S., Santos B.S., et al.: Fast Pulmonary Contour Extraction in X-ray CT Images: A Methodology and Quality Assessment. SPIE - Medical Imaging: Physiology and Function from Multidimensional Images, Vol. 4321. SPIE - The International Society for Optical Engineering, U.S.A, 2001, pp. 216-224.

17. Lopez C.A., Fernandez M.M., Alzola J.R.: Comments on: A Methodology for Evaluation of Boundary Detection Algorithms on Medical Images. IEEE Transactions on Medical Imaging, 2004, vol.23, pp. 658-660.

18. Chalana V., Kim Y.: A Methodology for Evaluation of Boundary Detection Algorithms on Medical Images. IEEE Transactions on Pattern Analysis and Machine Intelligence, 1997, vol.16, pp. 642-652.

19. Byrd K.A., Zeng, J., Chouikha, M.: A Validation model for segmentation algorithms of digital mammography images. Journal of Applied Science & Engineering Technology,2007, vol.1, pp. 41-50.

20. Pu J. et al.: A Computational Geometry Approach to Automated Pulmonary Fissure Segmentation in CT Examinations, IEEE Transactions on Medical Imaging, 2009, vol. 28, pp. 710-719.

21. Zuiderveld K.: Contrast Limited Adaptive Histograph Equalization. Graphic Gems IV, San Diego: Academic Press Professional, 1994, pp. 474–485.

22. (2010, July) [Online]: http://www.mathworks.com/help/toolbox/images/ref/adapthisteq.html

23. (2010, July) [Online]:http://radonc.ucsf.edu/research_group/jpouliot/tutorial/HU/Lesson7.htm

24. (2010, July) [Online]:http://pt.scribd.com/doc/23192243/Cap20-Interpolacao-por-splines

25. (2010, July) [Online]:http://www.physics.utah.edu/~detar/phys6720/handouts/cubic_spline/cubic_spli ne/node1.html

26. Santos B., Ferreira C., Silva J., et al: Quantitative Evaluation of a Pulmonary Contour Segmentation Algorithm in X-ray Computed Tomography Images. Academic Radiology, 2004, vol.11, Nº 8, pp. 868-878.

27. (2010, July) [Online]:http://upload.wikimedia.org/wikipedia/commons/8/89/Boxplot_vs_PDF.png

28. (2010, July) [Online]:https://sites.google.com/site/marcosfs2006/boxplot

29. (2010, July) [Online]:http://regentsprep.org/REgents/math/ALGEBRA/AD3/boxwhisk.htm

30. (2010, July) [Online]:http://edndoc.esri.com/arcobjects/8.3/Samples/Analysis%20and%20Visualizatio n/Cluster%20Analysis/CLUSTERANALYSIS.htm

31. Holland S.M.: Cluster Analysis. University of Georgia, Athens, GA 30602-2501, 2006.

32. Kaufman L., Rousseeuw P.J.: Finding Groups in Data: An Introduction to Cluster Analysis. Wiley, New York, 1990.

33. (2010, July) [Online]:http://www.skillstat.com/heartscape/chambers.htm

34. Sun W., Cetin M., Chan R. Et al: Segmenting and Tracking the Left Ventricle by Learning the Dynamics in Cardiac Images. G.E. Christensen and M. Sonka (Eds.): IPMI 2005, LNCS 3565, 2005, pp. 553–565.

35. Zhu Y., Papademetris X., Sinusas A. J. et al: Segmentation of the Left Ventricle From Cardiac MR Images Using a Subject-Specific Dynamical Model. IEEE Transactions on Medical Imaging, 2010 Vol. 29, nº. 3, pp. 669-687.

36. (2010, July) [Online]:http://www.accessexcellence.org/AE/AEC/CC/heart_anatomy.php

37. Marieb E.N., Hoehn K. : Human Anatomy & Physiology. Benjamin Cummings, 7 edition, 2008.

38. (2010, July) [Online]:http://www.texasheart.org/hic/anatomy/anatomy2.cfm

39. (2010, July) [Online]:http://www.bostonscientific.com/lifebeat-online/heart-smart/congenital-heart-disease.html

40. (2010, July) [Online]:http://www.aptec.pt/cardiopneumologia/areas-de-intervencao/21-ecocardiografia-transtoracica-.html

41. Rahko P.S.: Echocardiography and Doppler Echocardiography. Encyclopedia of Medical devices and instrumentation, Second Edition, Volume 3, Jonh Wiley & Sons 2006.

42. (2010, July) [Online]:http://folk.ntnu.no/stoylen/strainrate/Ultrasound/#ultrasound

43. Webb A.G. :Introduction to Biomedical Imaging. IEEE Press Series on Biomedical Engineering, 2003.

44. (2010, July) [Online]:http://www.aium.org/aboutaium/history/timeline.aspx

45. (2010, July) [Online]:http://www.edurad.in/archives-ppt/ULTRASOUND/ULTRASOUND-ARTEFACTS.pdf

46. (2010, July) [Online]:http://www.us-tip.com/serv1.php?type=art

47. (2010, July) [Online]:http://anpat.unipd.it/ARVC/protocols/

48. (2010, August) [Online]:http://schools.medphys.ucl.ac.uk/images/images.html

49. (2010, August) [Online]:http://www.cmj.org/paper_journal/05/21/16/F052116_1.htm

50. Suri, J.S., Setarehdan, S.K., Singh, S.: Advanced algorithmic approaches to medical image segmentation: state-of-the-art application in cardiology, neurology, mammography and pathology. Springer-Verlag New York,2002.

51. Jacob G., Noble J.A., Behrenbruch C., et al.: A shape-space-based approach to tracking myocardial borders and quantifying regional left-ventricular function applied in echocardiography. IEEE Transactions on Medical Imaging, 2002 vol.21, pp. 226-238.

52. Noble J.A., Boukerroui D.: Ultrasound Image Segmentation: A Survey. IEEE Transactions on Medical Imaging, 2006, vol.25, pp. 987-1010

53. Bosh J.G. al.: Automatic Segmentation of Echocardiographic Sequences by Active Appearance Motion Models. IEEE Transactions on Medical Imaging, 2002, vol.21, pp. 1374-1383

54. Osher S., Sethian J.A.: Fronts Propagation with Curvature Dependent Speed: Algorithms Based on Hamilton-Jacobi Formulations. Journal of Computational Physics,1988, vol.79, pp. 12-49

55. Nadernejad E. et al.: Despeckle Filtering in Medical Ultrasound Imaging. Contemporary Engineering Sciences, 2009, vol. 2, pp.17-36.

56. Sudha S., Suresh G., Sukanesh R.: Speckle Noise Reduction in Ultrasound Images Using Context-based Adaptive Wavelet Thresholding. IETE Journal of Research, 2009, vol. 55, pp. 135-143.

57. Nascimento J., Sanches J.: Ultrasound imaging LV tracking with adaptive window size and automatic hyper-parameter estimation. 15th IEEE International Conference on Image Processing, 2008, pp. 553-556.

58. Jarur M.C., Mora M.: Heart cavity detection in ultrasound images with SOM. 5th Mexican international conference on artificial intelligence, 2006. pp. 1211-19.

59. Bansod P., Desai U.B., Burkule N.: Multi Frame Guided Local Search for Semiautomatic Endocardial Contour Estimation in Echocardiography Sequences. 6th International Conference on Information, Communications & Signal Processing. Singapore, 2007. pp. 1-5.

60. Valdes-Cristerna R. et al: Texture-based echocardiographic segmentation using a non-parametric estimator and an active contour model. 26th Annual International Conference of the IEEE Engineering in Medicine and Biology Society, San Francisco, 2004. pp. 1806-1809.

61. (2010, August) [Online]:http://www.mathpages.com/home/kmath109/kmath109.htm

62. (2010, August) [Online]:http://www.mathworks.com/help/techdoc/learn_matlab/f3-40352.html

63. Littlefield R., Macedonia C., Coleman J.: MUSPAC 3-D ultrasound telemedicine/telepresence system. In Proc. IEEE Ultrasonics Symposium, 1998, vol. 2, pp. 1669-1675.

64. Kontaxakis G., Walter S., Sakas G.: Eu-teleinvivo: An integrated portable telemedicine workstation featuring acquisition, processing and transmission over low-bandwith lites of 3-D ultrasound volume image. In Proc. Information Technology Applications in Biomedicine (ITAB), 2000, pp. 158–163.

65. Pierrot F. et al: Hippocrate: A safe robot arm for medical applications with force feedback. Med. Image Anal., 1999, vol. 3, pp. 285–300.

66. Abolmaesumi P. et al: A user interface for robot-assisted diagnostic ultrasound. IEEE Int. Conf. Robotics and Automation (ICRA), 2001, pp. 1549–1554.

68. Cunha D. et al: The midstep system for ultrasound guided remote telesurgery. Proc. 20th Annu.Int. Conf. IEEE Engineering in Medicine and Biology Society, 1998, pp.1266–1269.

69. Mitsuishi M. et al: Remote ultrasound diagnostic system. Proc. IEEE Int. Conf. Robotics and Automation. 2001, pp.1567–1574.

70. Gourdon A. et al: Master–slave robotic system for ultrasound scanning. Proc. Eur. Medical and Biological Engineering Conf., vol. II, Mar. 1999, pp.1116–1117.

71. Masuda K. et al: Three-dimensional motion mechanism of ultrasound probe and its application for tele-echography system. in Proc. IEEE/RSJ Int. Conf. Intelligent Robots and Systems, 2001, pp. 1112–1116

72. Vilchis A. et al: A new robot architecture for Tele-Echography. IEE Transactions on Robotics and Automation, vol. 19, nº5, 2003, pp. 922-926.

73. (2010, August) [Online]:http://www.vecna.com/robotics/solutions/wam_arm.shtml

74. (2010, August) [Online]:http://www.sonomahealth.com/sonosite-titan.html

75. (2010, August) [Online]:http://www.inition.com.au/inition/dispatcher.php?action=get&model=products&URL_=product_ffhaptic_sensable_phantomdesktop&SubCatID=0&tab=blurb

76. Sousa C., Cortesão R., Santos L.: Computed Torque Posture Control for Robotic-Assited Tele-echography, 18th Mediterranean Conference on Control and Automation, 2010, pp. 1561-1566.

77. Pal N. R., Pal S.K.: A review on image segmentation techniques. Pattern Recognition 1993, vol.26, pp. 1277–1294.

78. Pham D., Xu C., Prince J.: Current methods in medical image segmentation. Annual Review Biomedical Engineering, 2000, vol.2, pp.315–337.

79. Hoover A. et al: An experimental comparison of range image segmentation algorithms. IEEE Transactions on Pattern Analysis and Machine Intelligence, 1996, vol.18, pp. 673–689.

80. Zhang Y.: A survey on evaluation methods for image segmentation. Pattern Recognition, 1996, vol.29, pp.1335–1346.

81. Bowyer K.: Validation of medical image analysis techniques. In: Beutel J, Kundel H., Metter Rvan, editors. The Handbook of Medical Imaging, SPIE, 2000.

82. Loughlin M. et al.: Three-dimensional modeling of biopsy protocols for localized prostate cancer, Computerized Medical Imaging Graphics, 1998, vol.22, pp.229–238.

83. McFarland E. et al.: Spiral CT colonography: reader agreement and diagnostic performance with two- and three-dimensional image-display techniques. Radiology, 2001, vol. 218, pp. 375–383.

84. Udupa J. K.: A framework for evaluating image segmentation algorithms. Computerized Medical Imaging and Graphics, 2006, vol.30, pp.75–87.

85. (2010, September) [Online]:http://www.mathworks.com/products/matlab/

86. Craig J.: Introduction to Robotics, Mechanics and Control. Third Edition, Pearson Education, Inc., 2005.

87. (2010, September) [Online]:http://home.dei.polimi.it/matteucc/Clustering/tutorial_html/kmeans.html